

MASTER'S THESIS



- Fluorophore detection in complex media **3**
- Build your own experiments **23**
- Supplementary materials **29**

EPFL

FRÉDÉRIC DE GOUMOËNS

I would like to express my gratitude to Prof. Moser, who gave me the opportunity to realize my thesis in a Lab of one of the most cutting-edge university in the world, at the Caltech's Biophotonics Laboratory. For their guidance, time and effort in helping me complete this Master's thesis, my sincere appreciation goes to Prof. Yang and Dr. Blochet. They have demonstrated a lot of patience in helping me learn the techniques and concepts used in this project and have always been present to answer my questions. Thank you.

Even if because of the COVID pandemic my stay there was shortened, it remained a very rewarding experience and I am really grateful for it.

A handwritten signature in black ink, reading "F. de Goumoëns". The signature is written in a cursive style with a large, stylized 'F'.

Frédéric de Goumoëns

Table of content

Three-dimensional localization of fluorophores	3
Introduction	3
Problem formulation	4
Light propagation	4
Parameters definition	5
2D Localization algorithm (2D-FADE)	6
3D Localization algorithm (3D-FADE)	8
Spatial interpolation	9
Types of modulation	11
Successive measurements	11
Simultaneous amplitude modulation	11
Simultaneous speckle modulation	12
Methods	15
Devices	15
Samples	16
Results	17
Discussion	20
Conclusion	21
References	22
Build your own experiments	23
EE005 - Introduction to waves	23
Mass-spring experiment	23
Twenty SHO chain	24
Sound waves and arduino	25
Forced oscillators and wine glass breaking	26
Smoke vortex cannon	27
Supplementary Information	29
1. System characterisation (full results)	29
2. Derivation of the temporal speckles superposition formula	30
3. Algorithms for generation of temporal speckles and computation of R	31
4. PCB Schematic	32
5. Group meeting slides	34

EPFL**Caltech**

Three-dimensional localization of fluorophores toward deep single-pixel imaging in complex media

FRÉDÉRIC DE GOUMOËNS,^{1,2,*} SUPERVISED BY BAPTISTE BLOCHET,¹
CHANGHUEI YANG,¹ AND CHRISTOPHE MOSER²

¹Electrical Engineering, California Institute of Technology, Pasadena, CA 91125, USA

²School of Engineering, Ecole Polytechnique Federale de Lausanne, CH-1015 Lausanne, Switzerland

*frederic.degoumoens@epfl.ch

Started 17 February 2020; submitted 11 September 2020; defended 18 September 2020

Imaging in complex media, such as biological tissues, has been for many years a challenge in the academic and industrial researches due to the rapid signal losses that preclude decent resolution. Many solutions were invented to fight the light's scattering and extract the information from the blurred measurements but they are often computationally heavy and the imaging depth remains very shallow. The working principle of recent techniques that use the localization of blinking fluorophores, as building block for 3D imaging, could potentially be used to increase the depth and resolution of detection in complex media. In this work, we present a simple fluorophore localization technique that allows real-time 3D tracking of particles in strongly diffusing media. Our method has the potential to determine the absolute position of fluorescent particles in any media without a priori knowledge on its optical properties. This was achieved by using a single-pixel imaging setup with an illumination array where each light source can be individually modulated and used to emit specific patterns. A proof of concept device has been made from off-the-shelf components and has shown millimetric accuracy beyond the transport mean free path (i.e. 20 scattering mean free paths). Our results might pave the way to high resolution photo-activated localization imaging at greater depths than current techniques. © 2020

Introduction

When it comes to imaging or detecting objects in scattering media, the different techniques used can usually be divided into two categories: ballistic and non-ballistic imaging. Ballistic methods want to suppress the scattered photons to keep only the unscattered (i.e. ballistic) light that went through the medium in a straight line. Most of the intensity (proportionally to the depth) has to be filtered out in the process, leaving only a reduced number of photons for detection. They typically allow for near diffraction-limited resolution or even down to 20 nm when using fluorophores [1]. Among these techniques are confocal imaging and optical coherence tomography (OCT). Confocal imaging, which uses a spatial gating to filter out the scattered photon, has a depth limit of one scattering mean free paths (l_s). By using a spatio-temporal gating, the OCT extends this range to approximately $27 \cdot l_s$ (~ 1 mm in soft tissues) [2]. Photo-activated localization microscopy (PALM), is an example of a method that uses fluorophores localization for super-resolution imaging. In conventional microscopy, the resolution is defined by the ability to spatially separate two light sources (i.e. fluorophores) and is limited by the light's diffraction. To achieve a resolution below this conventional limit, PALM utilizes blinking fluorophores which leads to temporal (instead of spatial) separation of the light sources. The resolution is then limited only by the localization efficiency of an individual fluorophore [3]. Nevertheless, like the other ballistic methods, PALM remains limited to a maximum depth of one l_s [1].

On the other side, non-ballistic imaging methods measure all the light, including the multiply scattered (MS) photons. The higher intensity signal allows to go deeper in the medium but the resolution is deteriorated by the randomization of the light. By sensing the intensity at specific locations, they can then reconstruct an image by modeling the light propagation in the medium (see [Light propagation](#) section). That is the working principle of photoacoustic tomography (PAT) [4] and diffuse optical tomography (DOT) [5], that are able to image deeper than $200 \cdot l_s$ (~ 10 mm in soft tissues) but with a resolution usually in the order of 100 μ m to 1 mm.

Another aspect of this work concerns single-pixel imaging. Unlike usual imaging setup, where a light source is

used to illuminate an object that is recorded by a camera with an array of $N \times N$ pixels, single-pixel imaging is instead using a $N \times N$ illumination array (usually a DMD) along with a single-pixel detector. The scene information is then obtained by applying a series of spatially resolved patterns on the illumination array and measuring the resulting intensity on the detector [6]. In our case we go a step further since we additionally assume that each individual pixel can be specifically modulated, independently from other pixels. Single-pixel imaging allows, under certain conditions, faster information recovery than traditional methods [7].

In regard to the current state of the art, there is a clear need for a trade-off between the high-resolution of ballistic techniques and the imaging depth of non-ballistic methods, while maintaining a high frame rate. In this work, we propose a fast algorithm for detection in deep diffuse environment (FAD³E, referred as FADE) that extends the super-resolution approach (fluorophores localization), combined with the single-pixel imaging capabilities, in the diffuse regime. To achieve this, we will first study the light propagation in complex media and determine the best way to model it analytically. We will then numerically simulate different localization strategies and finally build a setup to verify our models experimentally.

Problem formulation

Light propagation

The radiative transfer equation (RTE) is accepted as the equation that describes the light propagation in biological tissue [8], but the RTE cannot easily be solved analytically and the numerical solutions are computationally extremely heavy [5]. Under some assumptions (thickness $\gg l^*$ and $\mu_a \ll \mu'_s$) [9], the RTE can be simplified to the commonly used diffusion equation (DE), whose steady-state formulation [10–12] is

$$\mu_a \cdot I_{\text{dif}}(r) - D \cdot \Delta I_{\text{dif}}(r) = S(r) \quad (1)$$

where I_{dif} is the diffused intensity, $D = [3(\mu_a + \mu'_s)]^{-1}$ is the diffusion coefficient, μ_a and $\mu'_s = \mu_s(1 - g)$ are respectively the absorption and reduced scattering coefficients, g is the anisotropy and S the source intensity. Solving Eq. (1) in an infinite homogeneous medium for an isotropic point source [13], we find

$$I_{\text{dif}}(r) = I_0 \frac{1}{4\pi D} \frac{1}{r} \cdot e^{-\sqrt{3\mu_a\mu'_s} \cdot r} \quad (2)$$

where r represents the distance between the source and the detector. Assuming the source's position is known, multiple measurements of the distance r could allow to find the position of the detector. The DE provides a very good approximation of the RTE (Fig. 1.a), especially for depths greater than l^* . The remaining issue is that $r(I_{\text{dif}})$, the DE inverse function, cannot be expressed in terms of elementary functions [14]. To better model the propagation below l^* and to facilitate the inverse problem, we will consider the modified Beer–Lambert law (MBLL) [15, 16], an empirical description of the light propagation. The MBLL is widely used in instruments for continuous-wave near-infrared spectroscopy (cwNIRS), with applications such as breast imaging and brain function monitoring [5]. The MBLL is expressed as [17]

$$I(r) = I_0 \cdot e^{-\mu_a \cdot \text{DPF} \cdot r - G} \quad (3)$$

where G is a parameter that depends on the geometry and $\text{DPF} = L/r$ is the "differential pathlength factor" that corresponds to the ratio of the light mean pathlength (from source to detector) L over the source-detector distance r , with usual values between 3 and 6 [18]. Note that the DPF depends on r , μ_a and μ'_s [19], it then needs to be specifically selected for a given medium imaged at a selected depth (Fig. 1.b).

Even though the MBLL is the standard for cwNIRS, the limitations on the depth range imposed by the DPF make it unsuitable for some applications. In answer to this, a generalized Beer–Lambert law (GBLL) has been proposed [17] and is expressed as

$$I(r) = I_0 \cdot e^{-\bar{\mu} \cdot r} \quad , \quad \bar{\mu} = \mu_0 + \eta \frac{I}{I_0} \quad (4)$$

where $\bar{\mu}$ is called the total attenuation coefficient composed of two different attenuation coefficients μ_0 and η [17]. This simple model has proven to be accurate for large penetration depth (Fig. 1.c) and computationally more efficient since only two fixed parameters (μ_0 and η) can describes the light propagation at any depth in the medium [17]. Note that $\bar{\mu}$ varies with the intensity (i.e. with r) and that it is maximum ($\bar{\mu} = \mu_0 + \eta$) when $r = 0$ (i.e. $I = I_0$) and minimum ($\bar{\mu} = \mu_0$) when $r \rightarrow \infty$ (i.e. $I = 0$).

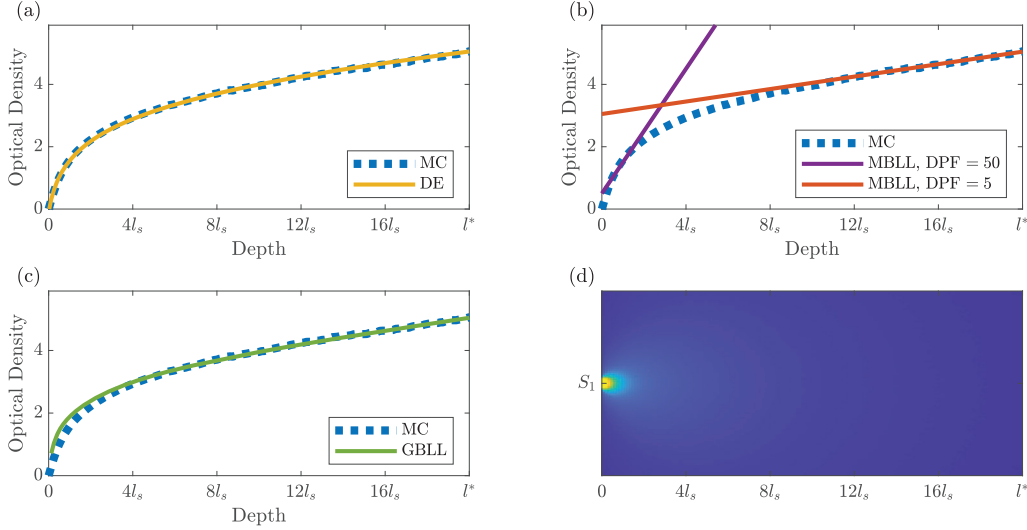


Fig. 1. Comparison of the different light propagation fitting methods with the MC simulation for $\mu_a = 0.005$ [mm^{-1}], $\mu_s = 0.25$ [mm^{-1}] and $g = 0.95$. The results are expressed in terms of optical density $OD = \ln(I/I_0)$. (a) Using the DE from Eq. (2). (b) Using the MBLL from Eq. (3), with $DPF = 50$, $G = 0.5$ and $DPF = 5$, $G = 3$. (c) Using the GBLL from Eq. (4), with $\mu_0 = 0.045$ and $\eta = 2.8$. (d) MC result.

To verify the accuracy of the different models, we commonly use a Monte Carlo (MC) method that computes the light propagation in a medium (with given optical properties) by statistically tracing the path of a large number of individual photons [20]. The MC method provides a numerical solution of RTE that is usually used as ground truth for simulations. We use it to compare the different equations presented in this introduction (Fig. 1). It appears that DE provides the best fitting of RTE but its mathematical complexity makes it unsuitable for most applications. The GBLL also fits well for a depth greater than $4 \cdot l_s$ but requires to determine the two parameters μ_0 and η beforehand and these are not directly related to the medium's coefficients (μ_a and μ'_s). The MBLL fitting, for a given DPF, only works for small depth's region of interest (ROI) but the DPF has a more obvious physical meaning, can be derived from the medium's coefficients and is already commonly used in cwNIRS instruments. For these reasons, the MBLL approximation method will be used in this study.

Parameters definition

In order to localize a fluorophore inside a complex media in three dimensions, we propose a model that reduces the problem down to two light sources and one detector (Fig. 2). The sources (S_1, S_2) with intensity I_0 are positioned on one surface of the medium with respective coordinates (x_1, y_1) and (x_2, y_2) . Note that the sources will always be either aligned horizontally (i.e. $x_1 = x_2$) or vertically (i.e. $y_1 = y_2$). If the sources are modulated, their output intensities are defined as $I_{S1} = I_0 \cdot f_1(t)$ and $I_{S2} = I_0 \cdot f_2(t)$, where $f_1, f_2 \in [0, 1]$. The unknown position of the fluorophore is (x_f, y_f, z_f) . I_f is the intensity on the fluorophore and the contribution to I_f from S_1 and S_2 are called I_1 and I_2 respectively. We then have

$$I_f = I_1 + I_2 + 2\sqrt{I_1 I_2} \cdot \cos(\Delta\phi) \quad (5)$$

where the last terms is due to interference and only occurs when the sources are coherent. It is also important to mention that the fluorescent feedback sensed on the single-pixel detector, called I_D , is directly proportional to I_f . The detector has to be designed to recover as much as possible of the fluorescent light (using specific optics). For a complex homogeneous medium that absorbs/scatters light and considering isotropic sources, we expect to find

$$I_i = I_{Si} \cdot A(r_i, \mu_a, \mu'_s) = I_0 \cdot f_i(t) \cdot A(r_i, \mu_a, \mu'_s) \quad i \in [1, 2] \quad (6)$$

where $r_i = \sqrt{(x_f - x_i)^2 + (y_f - y_i)^2 + z_f^2}$ is the source-fluorophore distance. $A(r_i, \mu_a, \mu'_s)$ represents the light extinction in a given material (multiple models exist, see [Light propagation](#)). We also define the intensity ratio R (time-independent) at the fluorophore location as

$$R = \frac{I_1}{I_2} = \frac{A(r_1, \mu_a, \mu'_s)}{A(r_2, \mu_a, \mu'_s)} \quad (7)$$

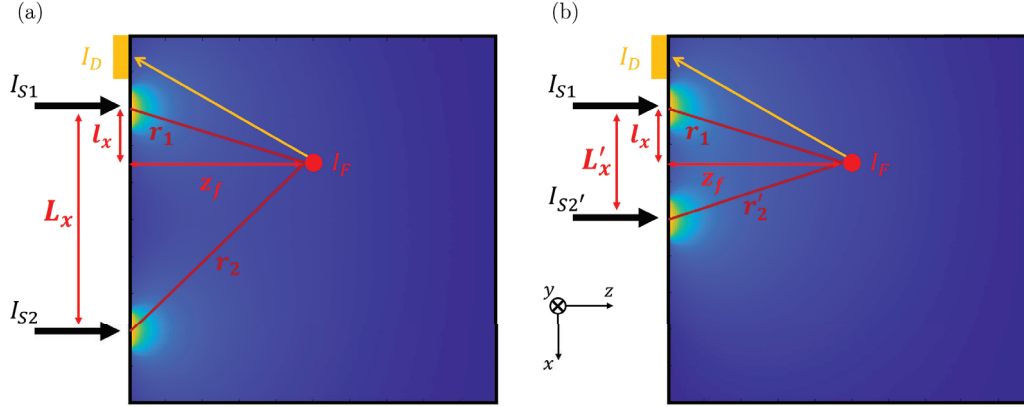


Fig. 2. 2D view of the light propagation from two sources in a complex media, showing the different parameters. The black arrows represent the light sources, the red dot is the fluorophore and the orange rectangle represent the light intensity sensor. (a) Example of sources positioning for the first measurement and (b) for the second measurement.

which represents the contribution from both sources to the fluorescent intensity I_f . Depending on $f_1(t)$ and $f_2(t)$, this ratio R can be found from the measured intensity I_D . More about that in the next sections (see [Types of modulation](#)). For now, we assume that R is known.

Finally, the separation between the sources along the x and y axis are $L_x = x_1 - x_2$ and $L_y = y_1 - y_2$ and we similarly define the distance between the fluorophore and the source S_1 as $l_x = x_f - x_1$ and $l_y = y_f - y_1$.

2D Localization algorithm (2D-FADE)

Since we know the position of S_1 , determining the 2D position (x_f, z_f) of the fluorophore is equivalent to finding l_x and r_1 by using

$$x_f = x_1 + l_x \quad z_f = \sqrt{r_1^2 - l_x^2} \quad (8)$$

In order to determine l_x and r_1 we can use the intensity ratio R (Eq. (7)) in which we insert the MBLL (Eq. (3)), giving

$$R = \frac{I_0 \cdot e^{-\mu_a \cdot \text{DPF} \cdot r_1 - G}}{I_0 \cdot e^{-\mu_a \cdot \text{DPF} \cdot r_2 - G}} = \frac{e^{-\mu_a \cdot \text{DPF} \cdot r_1}}{e^{-\mu_a \cdot \text{DPF} \cdot r_2}} = \frac{e^{-\mu_a \cdot \text{DPF} \cdot r_1}}{e^{-\mu_a \cdot \text{DPF} \cdot \sqrt{r_1^2 + L_x^2} - 2L_x l_x}} \quad (9)$$

$$\Rightarrow r_1 \cdot \left(\frac{2 \ln(R)}{\mu_a \cdot \text{DPF}} \right) - l_x \cdot (2L_x) = L_x^2 - \left(\frac{\ln(R)}{\mu_a \cdot \text{DPF}} \right)^2 \quad (10)$$

where $r_2 = \sqrt{r_1^2 + L_x^2} - 2L_x l_x$ is found by simple trigonometry. Assuming the optical properties of the material are known, we then have one equation (Eq. (10)) with two unknowns (l_x and r_1). At least a second (non-trivial) equation is needed to solve the system, meaning that we need to make a second measurement of the intensity ratio (R') for a different distance between the sources (L'_x , see Fig. 2.b), which gives us

$$\begin{cases} r_1 \cdot \left(\frac{2 \ln(R)}{\mu_a \cdot \text{DPF}} \right) - l_x \cdot (2L_x) = L_x^2 - \left(\frac{\ln(R)}{\mu_a \cdot \text{DPF}} \right)^2 \\ r_1 \cdot \left(\frac{2 \ln(R')}{\mu_a \cdot \text{DPF}} \right) - l_x \cdot (2L'_x) = L_x'^2 - \left(\frac{\ln(R')}{\mu_a \cdot \text{DPF}} \right)^2 \end{cases} \quad (11)$$

leading to

$$r_1 = \frac{1}{2\mu_a \cdot \text{DPF}} \cdot \frac{L_x \ln(R')^2 - L_x' \ln(R)^2 + \mu_a^2 \cdot \text{DPF}^2 \cdot [L^2 \cdot L_x' - L_x \cdot L_x'^2]}{L_x' \ln(R) - L_x \ln(R')} \quad (12)$$

$$l_x = \frac{1}{2\mu_a^2 \cdot \text{DPF}^2} \cdot \frac{\ln(R) \ln(R')^2 - \ln(R)^2 \ln(R') + \mu_a^2 \cdot \text{DPF}^2 \cdot [L_x^2 \ln(R') - L_x'^2 \ln(R)]}{L_x' \ln(R) - L_x \ln(R')} \quad (13)$$

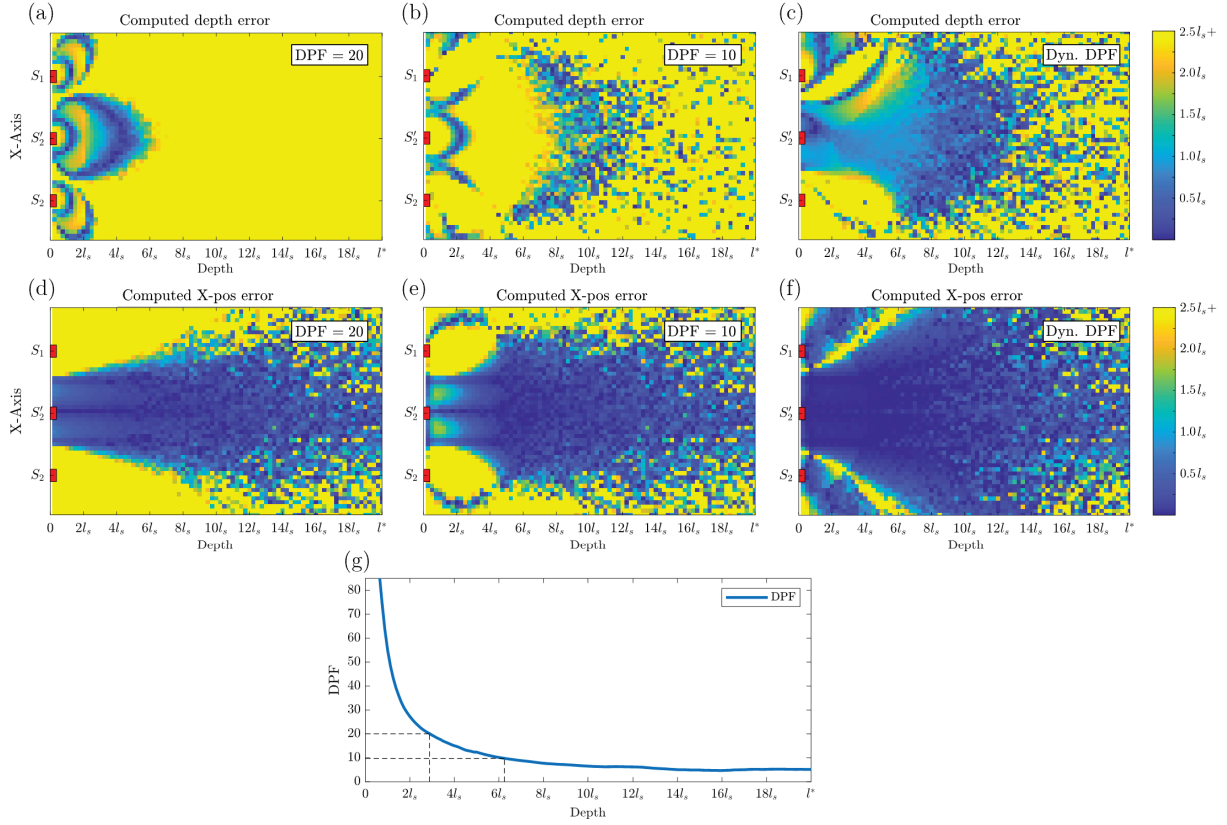


Fig. 3. Simulation results for the localization's absolute error of Eq. (12) and Eq. (13) down to l^* . These results were computed using the MC simulation (see Fig. 1 for details) for $L_x = 30$ mm and $L'_x = 15$ mm. The first row shows the error on the depth for (a) DPF = 20, (b) DPF = 10 and for (c) a dynamically selected DPF based on (g) the DPF values obtained by fitting the MC simulation on a $0.5l_s$ ROI with the MBLL. The second row shows similar results for the X-position error.

The localization's accuracy of Eq. (12) and Eq. (13) has been verified numerically on the MC simulation for different values of the DPF (Fig. 3). The results show that for a given DPF (e.g. Fig. 3.a), the localization is only accurate on a small ROI. Using a dynamic DPF (e.g. Fig. 3.c) allows to extend this ROI. In the [Spatial interpolation](#) section, we show that the DPF can also be determined dynamically without a priori on the medium's properties. It also appears that the lateral positioning (i.e. X-pos) error (Fig. 3.d-f) remains accurate for a thin but deep ROI aligned with the central source S'_2 . Note that the spacing between the sources has to be large enough to generate a good intensity contrast between I_1 and I_2 but small enough so that the selected DPF can be valid for both the r_1 and r_2 distances.

In the previous results (Fig. 3), we considered that R was known and noise free. In practice, R measurements are always subject to noise that will impact the results. Using the propagation of uncertainty formula, we compute the noise on the distance (σ_{r_1}) and on the position (σ_{l_x}) vs the signal-to-noise ratio of the R measurements ($\text{SNR}_R = R/\sigma_R$). To simplify, we assume that $L = L'$ and that R and R' are subject to the same noise σ_R .

$$\sigma_{r_1} = \sqrt{\left(\frac{\delta r_1}{\delta R}\right)^2 \sigma_R^2 + \left(\frac{\delta r_1}{\delta R'}\right)^2 \sigma_R^2} = \frac{\sqrt{R^2 + R'^2}}{2RR'\mu_a \text{DPF}} \sigma_R \stackrel{R=R'}{=} \frac{1}{\sqrt{2}\mu_a \text{DPF}} \cdot \frac{1}{\text{SNR}_R} \quad (14)$$

and similarly

$$\sigma_{l_x} = \sqrt{\left(\frac{\delta l_x}{\delta R}\right)^2 \sigma_R^2 + \left(\frac{\delta l_x}{\delta R'}\right)^2 \sigma_R^2} = \frac{|\ln(R)|}{\sqrt{2}L(\mu_a \text{DPF})^2} \cdot \frac{1}{\text{SNR}_R} \quad (15)$$

The $1/\text{SNR}_R$ dependence of the localization's error can be verified numerically for the depth and lateral position (Fig. 4). A threshold on the SNR_R can then be found and a minimum value of $\text{SNR}_R = 50$ is required to keep the error below a few millimeters. This can be achieved by most optical detectors.

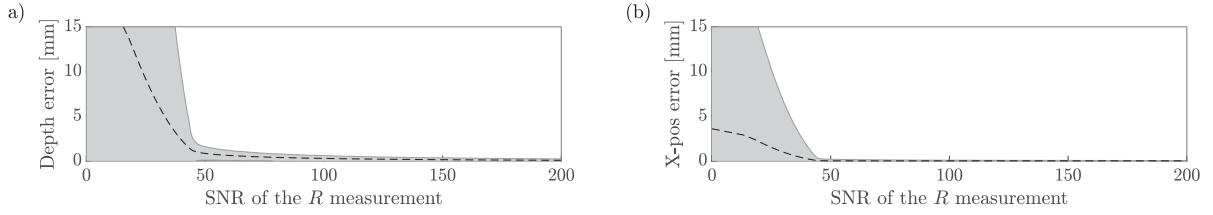


Fig. 4. Numerical simulation of the SNR_R 's effect on the (a) depth absolute error and (b) lateral position absolute error. The MC solver (c.f. Fig. 1) with added noise was used to generate the results. The positions were computed using Eq. (12,13) with a DFP of 20 (see Fig. 3.a,d) and the fluorophore was placed in the middle of the ROI.

3D Localization algorithm (3D-FADE)

The theory developed for the 2D-FADE can easily be extended to three dimensions by doing the measurements for the xz plane (giving l_x and r_1) followed by the yz plane (giving l_y and r_1). On Fig. 5 we show a generic step-by-step procedure to compute the fluorophore's 3D position.

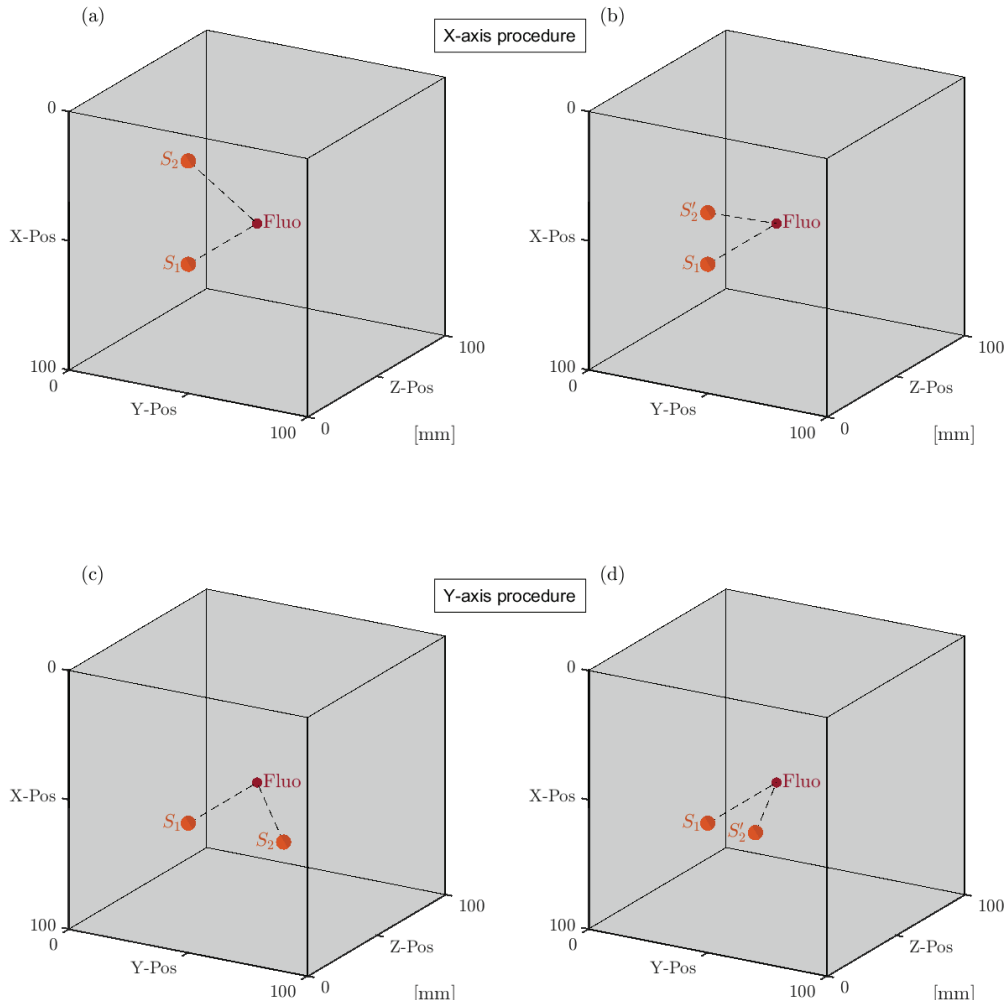


Fig. 5. Sources placement procedure for the 3D-FADE localization where the sources are shown in orange and the fluorophore is in red. (a) First measurement, along the X-axis. (b) Second measurement, along the X-axis. (c) Third measurement, along the Y-axis. (d) Fourth measurement, along the Y-axis.

Note that the source S_1 has to be approximately placed on top of the fluorophore (i.e. $x_1 \approx x_f$ and $y_1 \approx y_f$) in order for the algorithm to work (more details in the next section).

Spatial interpolation

Mechanically moving the sources to the different places would require a rather complex actuation system and make the overall process very slow. Instead, a solution with an array of $N \times N$ sources where each source can be individually controlled electronically has been considered (Fig. 6.a). This configuration can be seen as a single-pixel imaging setup [7] since spatially resolved patterns are emitted by the illumination array and the fluorescent feedback is sensed by a single-pixel detector (Fig. 6.b) to finally determine the position of the particle (Fig. 6.d).

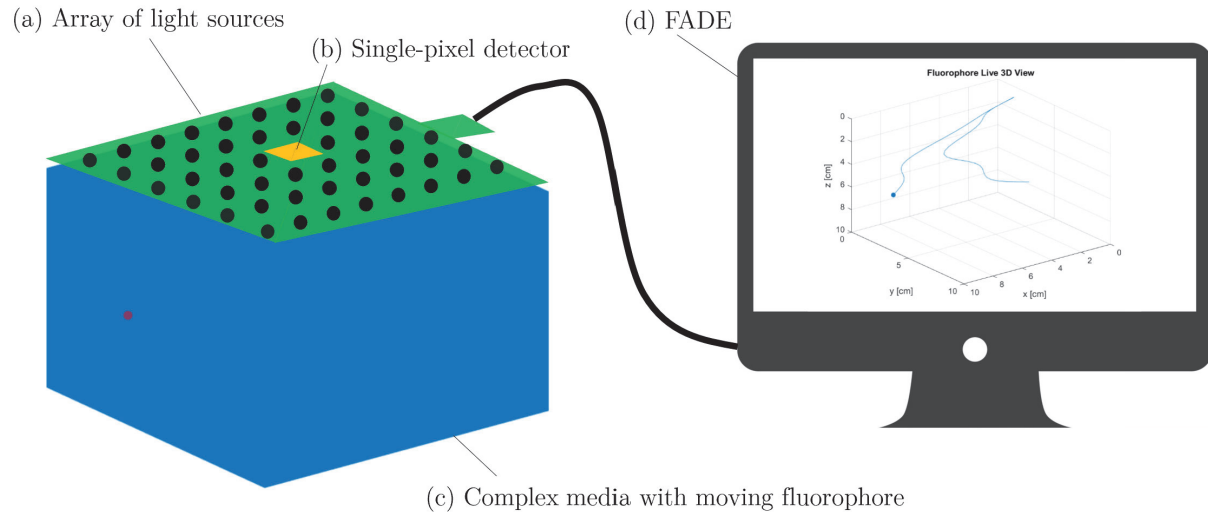


Fig. 6. Illustration of the fluorophore detection setup using (a) an array of sources where the placement of the light's emission can be electronically controlled. The 3D position of (c) the fluorophore moving in a complex media can be determined on (d) a computer running the FADE method. The fluorescent feedback is sensed by (b) a single pixel detector.

Using this configuration also enables new ways of determining the fluorophore position. In fact, similarly to PALM/STORM methods [21, 22], the xy position (no depth information) can be found by spatial interpolation on the single pixel image obtained. This is done by fitting a two-dimensional Gaussian on the data and by extracting its centroid which correspond to the fluorophore's xy position (Fig. 7).

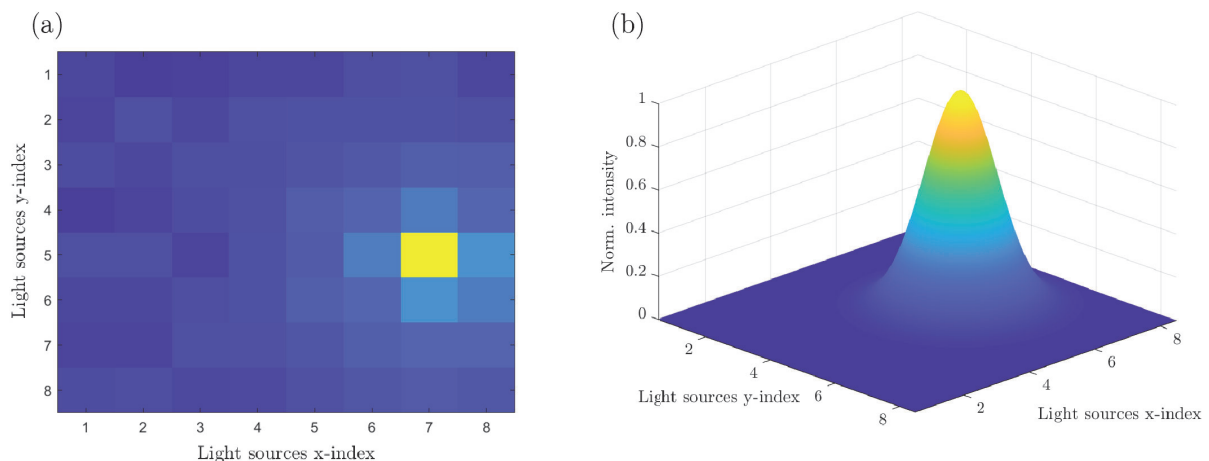


Fig. 7. (a) Exemple of raw intensity feedback generated by each of the light sources individually turned on. (b) The xy position of the particle is found by interpolating the results with a two-dimensional Gaussian.

Since the xy position can be accurately determined by spatial interpolation, the Eq. (13) in its actual form is no longer required for the localization procedure. More interestingly, since $l_x = x_f - x_1$ is now known, Eq. (13) can be used to dynamically obtain the μ_a DPF value. By rearranging the terms we obtain

$$\mu_a \text{DPF} = \sqrt{\frac{|\ln(R)^2 \ln(R') - \ln(R) \ln(R')^2|}{|L(L - 2l_x) \ln(R') - L'(L' - 2l_x) \ln(R)|}} \stackrel{l_x=0}{=} \sqrt{\frac{|\ln(R)^2 \ln(R') - \ln(R) \ln(R')^2|}{|L^2 \ln(R') - L'^2 \ln(R)|}} \quad (16)$$

where for simplification we considered that the source S_1 can be placed right on top of the fluorophore (i.e. $l_x = l_y = 0$). The dynamically found material dependent value can then be injected in the r_1 equation Eq. (12), leading to

$$r_1 = \frac{1}{2} \frac{|L(L - 2l_x) \ln(R')^2 - L'(L' - 2l_x) \ln(R)^2|}{\sqrt{|\ln(R)^2 \ln(R') - \ln(R) \ln(R')^2|} \cdot \sqrt{|L(L - 2l_x) \ln(R') - L'(L' - 2l_x) \ln(R)|}} \stackrel{l_x=0}{=} \frac{1}{2} \frac{|L^2 \ln(R')^2 - L'^2 \ln(R)^2|}{\sqrt{|\ln(R)^2 \ln(R') - \ln(R) \ln(R')^2|} \cdot \sqrt{|L^2 \ln(R') - L'^2 \ln(R)|}} \quad (17)$$

where r_1 is now only dependent on the R and R' measurements. Note that R and R' are computed using only the value of 3 specifically chosen sources (c.f. Fig. 5).

In practice, the xy positioning error generated by the interpolation will influence the accuracy of Eq. (16) and Eq. (17). The x and y positioning standard deviation (σ_x and σ_y) can be as high as $p/2$, where p is the spacing between each light source of the array. With the propagation of uncertainty formula, we compute the standard deviation in the measurements of $\mu_a \text{DPF}$ and r_1

$$\sigma_{\mu_a \text{DPF}} = \sqrt{\frac{1}{\text{SNR}_R^2} \frac{1}{2L^2} + \sigma_{xy}^2 \frac{\ln(R)^2}{L^4}} \quad (18)$$

$$\sigma_{r_1} = \frac{1}{(\mu_a \text{DPF})^2} \sqrt{\frac{1}{\text{SNR}_R^2} \left(\frac{(\mu_a \text{DPF})^2}{2} + \frac{\ln(R)^2}{2L^2} \right) + \sigma_{xy}^2 \frac{\ln(R)^4}{L^4}} \quad (19)$$

Note that $\mu_a \text{DPF} \ll 1 \text{ mm}^{-1}$, meaning that the noise on r_1 is amplified by $1/\mu_a \text{DPF}$ (in comparison with Eq. (14)) if the $\mu_a \text{DPF}$ value is dynamically determined. In both cases ($\sigma_{\mu_a \text{DPF}}$ and σ_{r_1}) the noise is inversely proportional to the signal-to-noise ratio of the R measurement (SNR_R), with an offset due the error on the x and y positioning (σ_{xy}). Based on the simulations results (Fig. 8), an accurate localization is now obtained under the condition that $\text{SNR}_R > 100$.

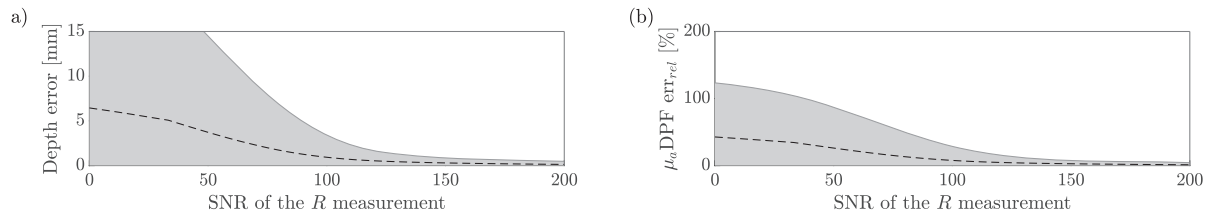


Fig. 8. Numerical simulation of the SNR_R 's effect on the (a) depth absolute error and (b) the computed $\mu_a \text{DPF}$ relative error. The MC solver (c.f. Fig. 1) with added noise was used to generate the results. The results were computed using Eq. (16,17). The l_x value was considered noise free.

Types of modulation

One of the main remaining challenge is to determine the value of the intensity ratio R as accurately as possible and with the minimum noise generation. It has to be determined using only the overall feedback I_D emitted by the fluorophore. In practice this can be done by applying different types of modulation to the S_1 and S_2 sources' intensity. Three types of modulation will be presented in the following sections. We will compare the accuracy/noise inherent to these modulation methods to finally determine the strengths and weaknesses of each of them.

Successive measurements

The first and more obvious type of modulation is to successive toggle the S_1 and S_2 sources (Fig. 9). Using that method, R can be directly computed by the ratio of the measured intensity when S_1 is on (S_2 off) over the intensity when S_2 is on (S_1 off). This is basically the working principle of the time-division multiplexing (TDM) used in telecommunications [23]. The sources being toggled alternatively, their light will never interfere, meaning both coherent and incoherent sources can be used.

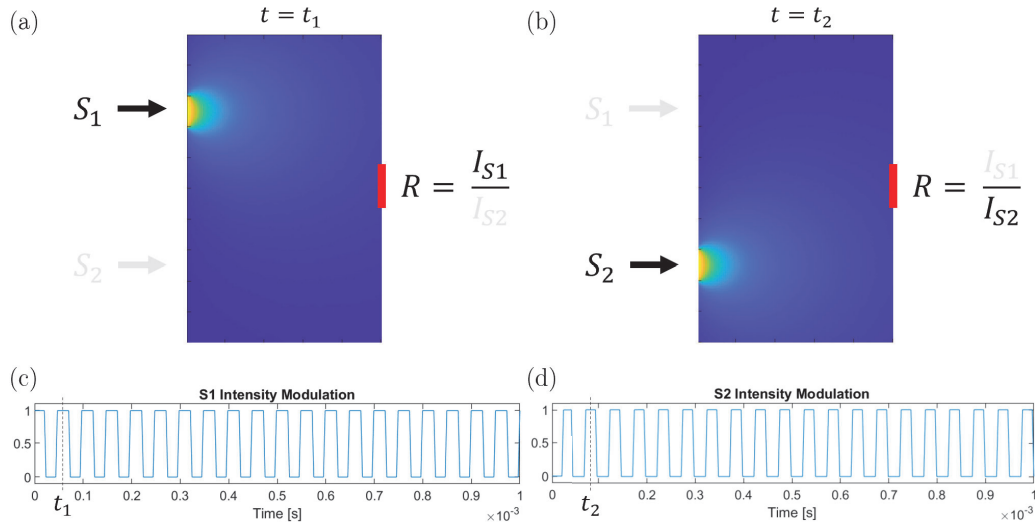


Fig. 9. Successive measurements method used to determine the intensity ratio R . The two sources S_1 and S_2 are alternatively turned on, producing different intensities on the fluorophore (red rectangle). (a) Light propagation in the medium when S_1 is on and (b) when S_2 is on. (c) Square modulation (20kHz) applied on S_1 and (d) on S_2 .

The main limitation of that method is that measurement conditions have to be identical when acquiring S_1 and S_2 intensities. If a perturbation would occur in between the two measurements (i.e. pressure change, macro molecules motion, etc.), the computed R will be wrong or noisy. This issue can be partially solved by increasing the source toggling frequency (Fig. 9.c,d).

Simultaneous amplitude modulation

A solution to reduce the impact of homogeneous temporal perturbations is to use the two sources simultaneously. Since sources will both be emitting at the same time, their light will be subject to the same perturbation in the medium which could improve the measurement of R . A common way to combine (i.e. multiplex) two signals while still being able to recover (i.e. demultiplex) the information carried by each of them is called frequency-division multiplexing (FDM) [24]. The information is separated by sinusoidally modulating (c.f. Fig. 10.b,c) the signals' amplitude with two frequencies f_1 and f_2 . The demultiplexing is done by extracting the associated frequency range in the superposed signals' spectrum (c.f. Fig. 10.d,e). Applied to our problem, this method allows us to find the intensity ratio with the relation

$$R = \frac{|F(f_1)|}{|F(f_2)|} = \frac{I_1}{I_2} \quad (20)$$

where $F(f)$ is the Fourier transform of the sensed intensity $I_D(t)$. Note that we considered that the two signals are not interfering. If the sources were coherent, harmonic frequencies would appear and the equation becomes

$$R = \frac{|F(f_1)|}{|F(f_2)|} = \frac{I_1 + \sqrt{I_1 I_2} \cos(\Delta\phi)}{I_2 + \sqrt{I_1 I_2} \cos(\Delta\phi)} \quad (21)$$

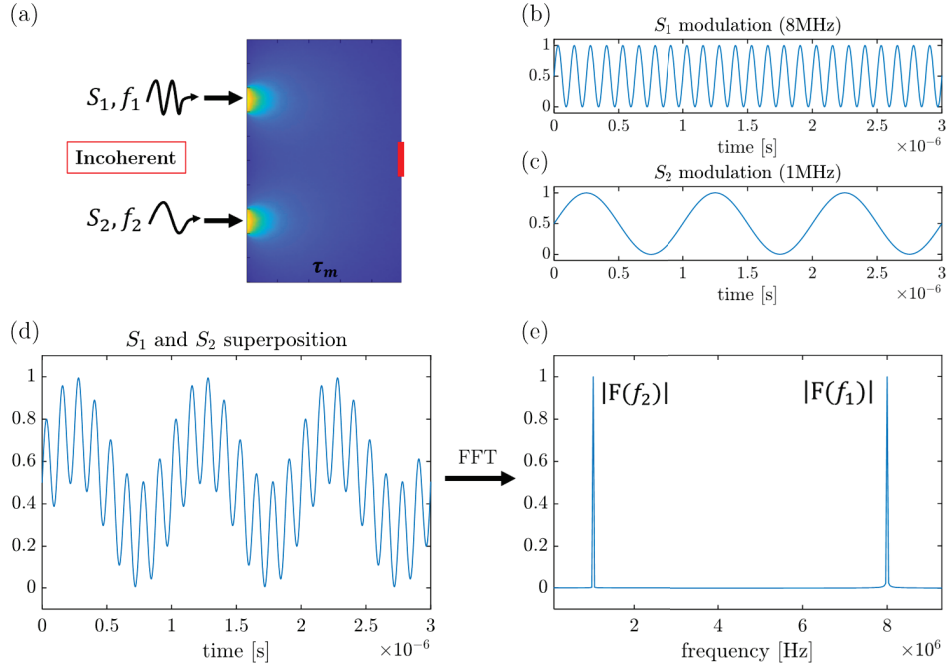


Fig. 10. Simultaneous measurements method with amplitude modulation used to determine the intensity ratio R . The superposed intensity from S_1 and S_2 is used to excite the fluorophore (red rectangle). (a) Visualization of the light propagation in the medium when both sources are on. (b) Sinusoidal modulation applied on S_1 (8MHz) and (c) on S_2 (1MHz). (d) Superposed intensity and (e) its Fourier transform.

which no longer gives the expected value of R . We will then only consider incoherent sources (e.g. LED).

This method (Fig. 10) is not sensitive to temporal perturbation in the medium and has the advantage of filtering out all the noise that has a frequency different than f_1 and f_2 . The implementation of such technique is more complicated and usually requires the use of a lock-in amplifier [25] to extract the amplitude of the respective frequencies.

Simultaneous speckle modulation

The last investigated method is more original since it uses temporal speckles as modulation. Speckles are deterministically randomized patterns generated when light travels through a scattering media [26]. When the medium moves (e.g. Brownian motion), the speckle pattern is altered, leading to the so-called temporal speckles (Fig. 11.a). A temporal speckle can be defined by its decorrelation time τ , representing the time it takes to completely modify its pattern. This is determined from the speckle autocorrelation function g_2 (Fig. 11.b) defined as [27,28]

$$g_2(t) = \frac{\langle I(t_0)I(t_0 + t) \rangle}{\langle I(t_0) \rangle \cdot \langle I(t_0 + t) \rangle} \quad (22)$$

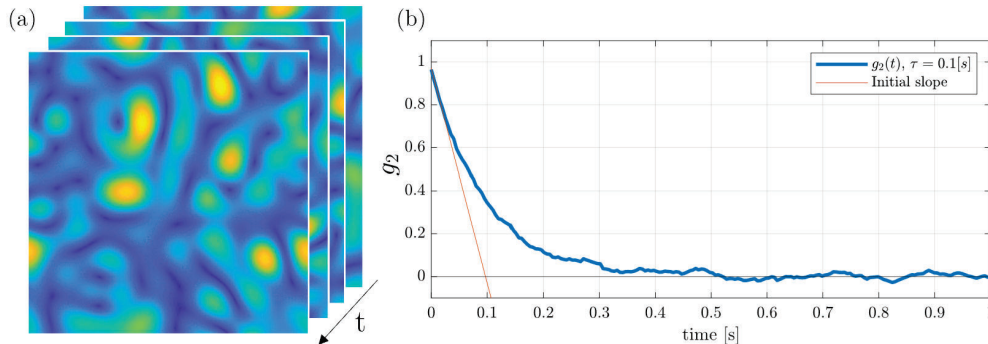


Fig. 11. (a) Brownian motion based time series of speckle patterns. (b) Autocorrelation function $g_2(t)$ from (a) with a decorrelation time of $\tau = 0.1$ s.

Depending on the type of medium's motion considered (Brownian, mechanical, etc.), $g_2(t)$ can have various

shapes (decreasing exponential, decreasing linear function, etc.) and the way of determining τ can vary. The most generic solution to find τ is to look at the initial slope of $g_2(t)$, i.e.

$$\tau = - \left[\frac{dg_2}{dt}(0) \right]^{-1} \quad (23)$$

The idea here would be to send two (specifically generated and known) speckle patterns with decorrelation times τ_1 and τ_2 inside of a scattering media (with decorrelation time τ_m). If $\tau_m \gg \tau_1$ and $\tau_m \gg \tau_2$, the media can be considered static and its effect on the speckle patterns is negligible. Similarly to the FDM, the superposition of temporal speckles can be used to multiplex the intensity of the sources. The resulting autocorrelation function $g_{2,tot}(t)$ of the superposed temporal speckles is found to be (see [Supplementary Section 2](#) for full derivation)

$$g_{2,tot}(t) = \left(\frac{I_1 \sqrt{g_{2,1}} + I_2 \sqrt{g_{2,2}}}{I_1 + I_2} \right)^2 \quad (24)$$

$$\tau_{tot} = \frac{(I_1 + I_2) \cdot \tau_1 \tau_2}{I_2 \tau_1 + I_1 \tau_2} \quad (25)$$

where $g_{2,1}$ and $g_{2,2}$ are the autocorrelation function of the two inputs, with the associated decorrelation times τ_1 and τ_2 . Note that the total autocorrelation $g_{2,tot}(t)$ function can be easily retrieved from the fluorescent intensity [29]. Since $g_{2,1}$ and $g_{2,2}$ are known, I_1 and I_2 (thus R), can be found by fitting of Eq. (24) on the measured $g_{2,tot}(t)$ (Fig. 12.a). This approach has shown great results (Fig. 12.b) as long as τ_1 and τ_2 are sufficiently different, meaning

$$\left| \frac{\tau_1 + \tau_2}{\tau_1 - \tau_2} \right| - 1 < T \quad (26)$$

where T is an arbitrary threshold that has to be selected to around 3 times the desired relative error on R as evaluated from experiments. Note that τ_1 and τ_2 have to be small enough to rapidly measure the autocorrelation function but large enough so that the detector can accurately sense the intensity variations. We found that $\tau_1 = 50$ ms and $\tau_2 = 500$ ms was a good compromise that led to less than 10% relative error on R .

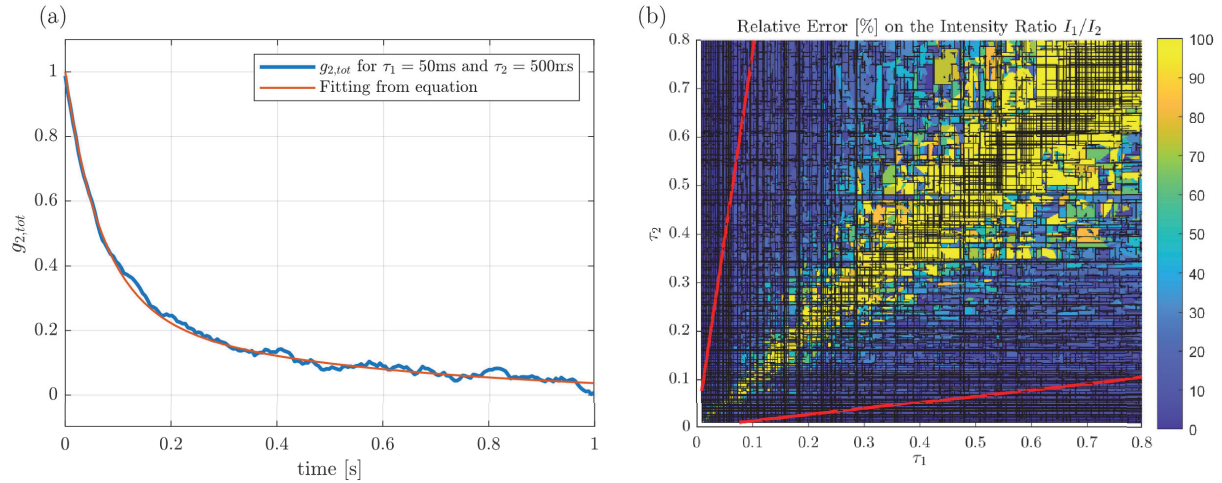


Fig. 12. Numerical results for the superposition of temporal speckles. (a) The total autocorrelation function $g_{2,tot}(t)$ generated by two (Brownian motion based) temporal speckles with $\tau_1 = 50$ ms and $\tau_2 = 500$ ms. (b) Relative error on R as a function of τ_1 and τ_2 . The red lines show the limit for 10% error.

Similarly to the simultaneous amplitude modulation, this method has the advantage of being insensitive to the homogeneous temporal perturbation in the media and can accurately find R under certain conditions. Nevertheless, the procedure for determining R is much more complicated than for the other methods and requires to numerically fit an equation (with two unknowns) on the measured data, which is computationally very heavy.

Comparison

To compare the efficiency of the three modulation methods on real case scenarios, we looked at their behaviour under simulated noise (Fig. 13). Two types of noise were tested : generic white noise and shot noise.

The generic white noise (Gaussian distribution) could represent thermal noise, flicker noise or amplification noise that are usually present in optical setups. Many ways to filter out this type of noise exist. The amplitude modulation is one of them (c.f. synchronous detection with lock-in amplifier [25]) which is why this method shows the less error in presence of white noise (Fig. 13.c).

The shot noise represents the only noise that technology will never be able to suppress since it is directly linked to the quantization of the photons. It becomes dominant when the number of photons available for detection gets low, which applies to our method as the (limited) intensity emitted by the fluorophore is drastically attenuated as it propagates through the medium. The shot noise follows a Poisson distribution, meaning that its standard deviation is equal to the square root of the mean intensity. Because of that, if a weak signal is multiplexed with a stronger one, the noise of the strong signal will make the weak one completely indiscernible.

This behaviour is clearly visible in the simultaneous amplitude modulation case (Fig. 13.d) where two sinusoids of different frequencies are summed up. Conversely, the successive measurement case (no superposition) shows a quasi perfect detection of R with shot noise (Fig. 13.b) but is strongly affected by the white noise since it is not able to filter any of it.

Remains the speckle modulation method that is also badly affected by white noise (no filtering) but shows decent results with shot noise. This method has been judged too complicated and without noticeable improvement in comparisons to the other modulation techniques.

Since the successive measurement methods is the simplest to implement and shows very good results in presence of shot noise, it is the one we decided to use for our experiments. If needed, synchronous detection with lock-in amplifier could still be applied on it to reduce the effect of low frequency noise.

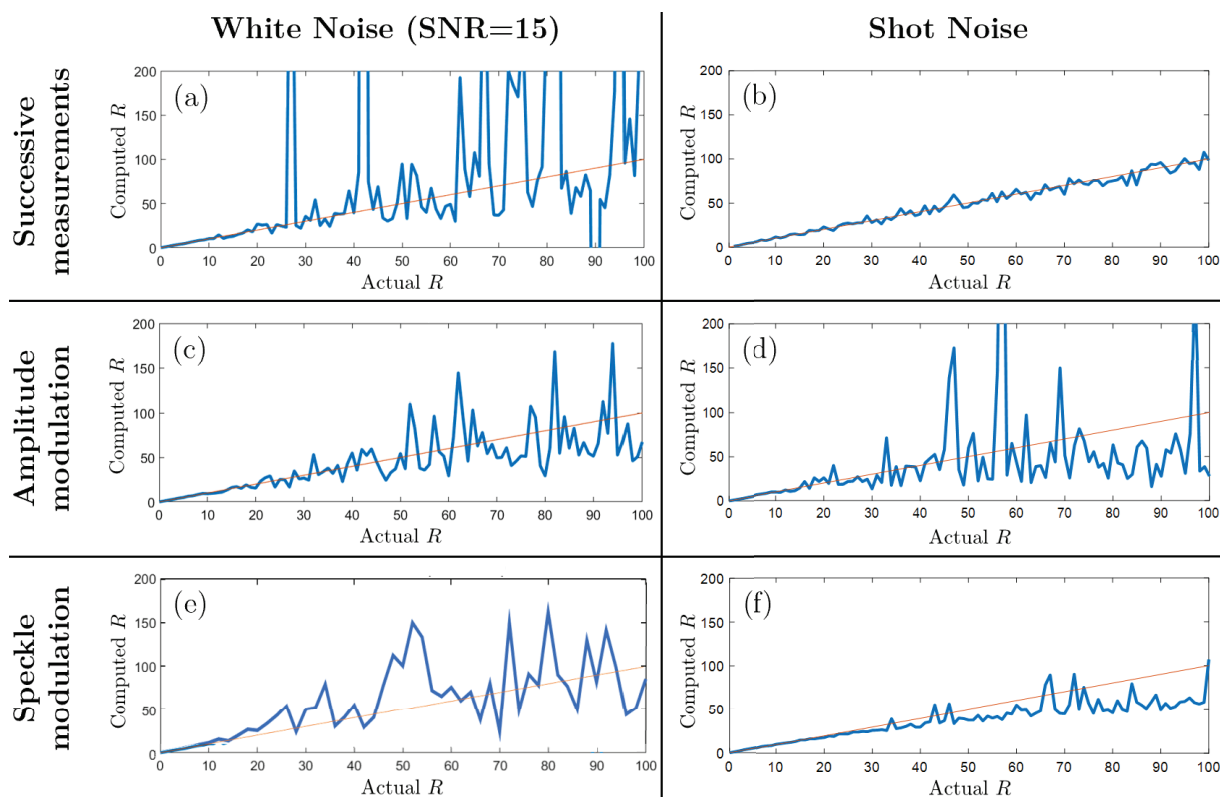


Fig. 13. Results of the noise analysis on the different modulation methods. The plots display the computed value of R versus the actual value, where the orange line is the reference. The first column shows the results for white noise (SNR=15) and the second shows the results in presence of shot noise.

Methods

In the previous sections, multiple theoretical methods were developed to determine the 3D position of a fluorescent particle. We introduced FADE, which is a set of equations based on the MBL that can be used to determine the depth of a fluorophore if provided with two intensity ratios (R and R') for different sources placement (Fig. 15.a). We showed that contrary to the light propagation fitting method, like the DE (see Fig. 15.b) or GBLL, the FADE method does not require to know the medium's optical properties to operate. We also demonstrated that the xy position of the particle can be determined by a spatial interpolation of the images obtained by single-pixel imaging. To verify if these methods could work in real applications, we have built a custom setup out of commonly available components (Fig. 14.a). *Design files are available in Supplementary Section 4.*

Devices

The illumination array (Fig. 14.c) uses 8×8 strong near-infrared (NIR) LEDs (*TSAL6100*, $\lambda = 940$ nm, $I = 170$ mW/sr, $\phi = \pm 10^\circ$, $t_r = 15$ ns) spaced by $p = 12.7$ mm and covering an overall surface of 10 cm by 10 cm. The NIR frequency takes advantage of the therapeutic window [30], minimizing the absorption for the targeted applications. Each of the NIR LED is paired with a visible red LED to provide a visual feedback on the other side of the array. The 64 sources are controlled using two 3 to 8 demultiplexers (*CD74HC238M96*), which allow to control each source independently using 6 logical inputs. Due to limited resources, we could not use fluorophores for the experiment. Instead, the intensity I_f the fluorophore would have received is directly sensed by an NIR photodiode (*BPW41N*, $\lambda = 870$ to 1050 nm, $\langle I_{reverse} \rangle = 45$ μ A, $\phi = \pm 45^\circ$) which we showed is equivalent since $I_f \propto I_D$ (see [Problem formulation](#)). We used digital potentiometers (*AD5242*, $R = 1$ M Ω , I^2C controlled) in a transimpedance amplifier circuit to dynamically modify the sensitivity of the probe, allowing to avoid saturation and to maximize the dynamic range of the measurements. To accurately move the probe in the medium while knowing its xyz absolute position, we designed a 3D ground truth measurement device (Fig. 14.e) out of 7 linear potentiometers. The main algorithms runs on a 8-bit AVR microcontroller (*ATmega2560*, Arduino Mega board, Fig. 14.d) which also actuates the array and senses the feedback from the probe. The processed xyz localization data are then transmitted via UART to a desktop computer that displays the information on a *Matlab* window. The complex medium is contained in a 10x10x10 cm watertight tank (Fig. 14.b) with a large opening on the top for the probe access and a thin transparent (2mm plexiglass) window on the front for the illumination array. All the rest of the tank has been covered in black (light absorbing) tape to prevent reflections and outside perturbation. It appeared for example that the NIR light was guided by total internal reflection inside the plexiglass frame of the tank and redistributed further in the medium, leading to very inaccurate measurements.

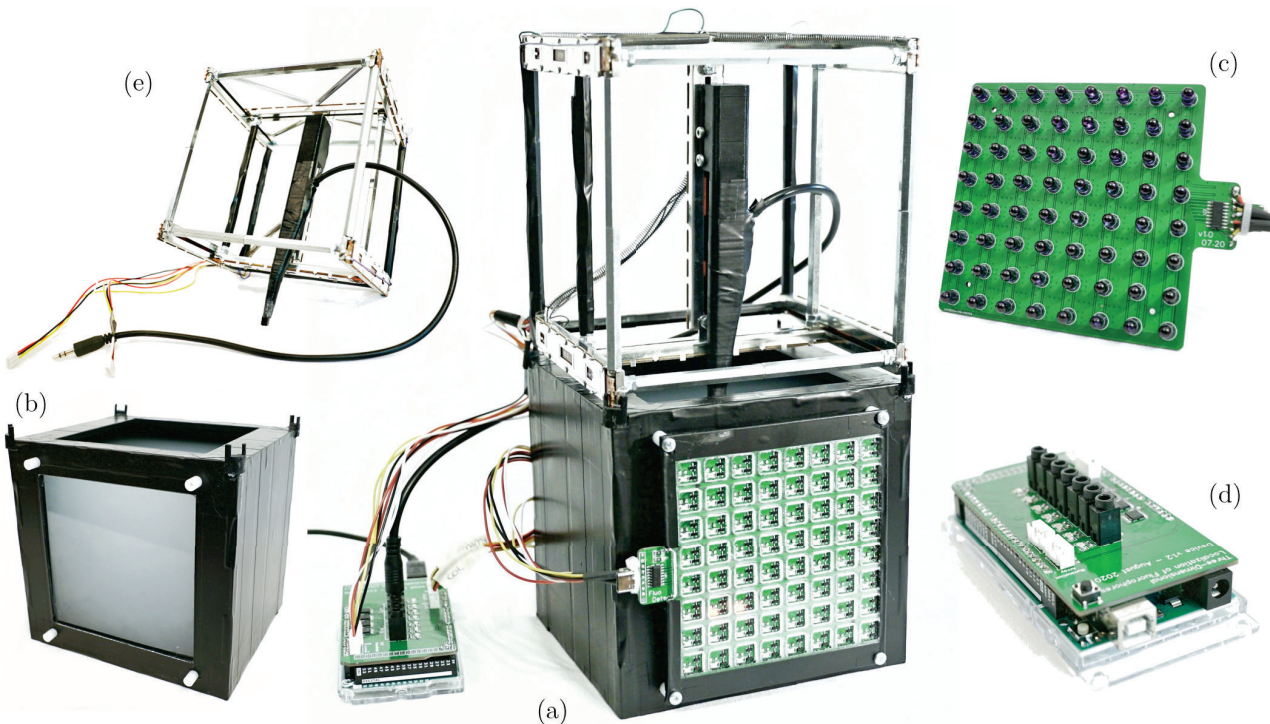


Fig. 14. Practical setup for the FADE proof of concept. (a) Assembled device. (b) Watertight tank filled with a liquid complex medium. (c) NIR illumination array. (d) Control board. (e) Ground truth measurement device.

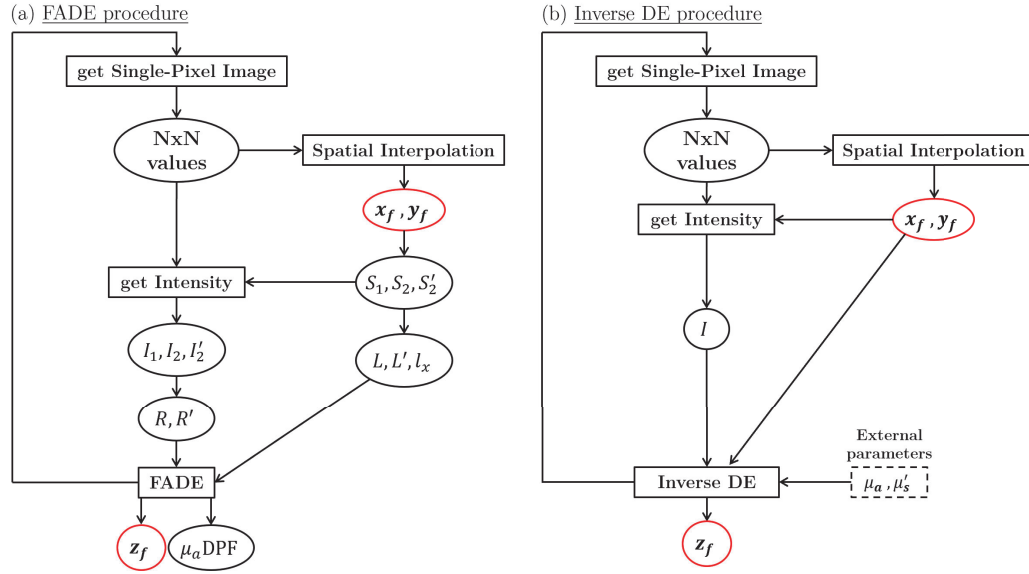


Fig. 15. Workflow diagrams for the (a) FADE procedure and (b) DE inverse function procedure. Both can be used to determine the localization of a fluorescent particle but the DE inverse function requires external parameters (μ_a, μ'_s) and uses the Lambert-W function. Conversely, the FADE procedure works in a closed loop.

Samples

To be able to freely move the probe inside of the tank, we had to find a liquid medium with convenient optical properties. We wanted a medium that strongly scatters the light (i.e. white) with minimum absorption. It appears that raw milk was the best option and its optical properties for 940nm NIR are well defined in the literature [31, 32]

$$\mu_{a,milk} \approx 0.01 \text{ mm}^{-1} \quad \mu_{s,milk} \approx 50 \text{ mm}^{-1} \quad g_{milk} \approx 0.95 \quad (27)$$

where its scattering properties mainly originate from the fat globules and casein proteins it contains.

Since our setup has much larger dimensions than the ones conventionally used in researches, we needed to extend the transport mean free path of the medium ($l^* = [\mu_s(1-g)]^{-1}$) to approximately the same dimension. From the Mie-theory [32] we know that

$$\mu_s = Q_s \cdot A \cdot N \quad (28)$$

where Q_s, A and N correspond respectively to the scattering efficiency, cross-section area and concentration of the scatterers in the medium. This means that μ_s can be reduced to any desired value by diluting the medium with another non scattering medium. The easiest way to do it is by diluting the raw milk in a given amount of deionized water (aqueous solution). Water has the advantage of not scattering the light (i.e. transparent) which makes it very suitable for this application. The water optical properties are also well defined in the literature [33, 34]

$$\mu_{a,water} \approx 0.035 \text{ mm}^{-1} \quad \mu_{s,water} \approx 0.2 \text{ } \mu\text{m}^{-1} \quad (29)$$

By diluting 10mL of raw milk in 2L of pure water (i.e. 5‰ solution), we obtain the solution we will use in our experiments. Using Eq. (28), the optical parameters of the solution are found to be

$$\mu_{a,sol} \approx 0.035 \text{ mm}^{-1} \quad \mu_{s,sol} \approx 0.25 \text{ mm}^{-1} \quad g_{sol} \approx 0.95 \quad (30)$$

$$l_{s,sol} \approx 2 \text{ mm} \quad l_{sol}^* \approx 80 \text{ mm} \quad (31)$$

where l_{sol}^* now correspond to around 80% of the device's maximum depth.

We realized that even if NIR light is the most suited for biological applications (c.f. therapeutic window [30]), it is much more absorbed by water than visible light (around 1'000 times more, see [34] for graphs). Using blue light would have been a wiser choice for the specific setup. We tried to use some other solvents with less absorption in the NIR range (like ethanol, methanol, gasoline, etc.) but none of them gave significantly better results.

Results

Using our custom setup, all our assumptions from the numerical simulations will be studied on a practical case. The mean value and standard deviation for each probe position is obtained from at least 40 measurements temporally spaced by approximately 0.1 s.

Intensity propagation

We first wanted to see how accurately the MC solver could simulate the light propagation in our medium (Fig. 16.a). By using the optical properties defined in Samples for the simulation, it appears that the propagation can be modeled by MC for any depths greater than $5l_s$ (i.e. 20mm).

The SNR of the R measurement, which can strongly influence the quality of the results (c.f. Fig. 4 and 8), is also presented (Fig. 16.b). We find that it has a mean value of around 50 and tends to decrease for greater depths.

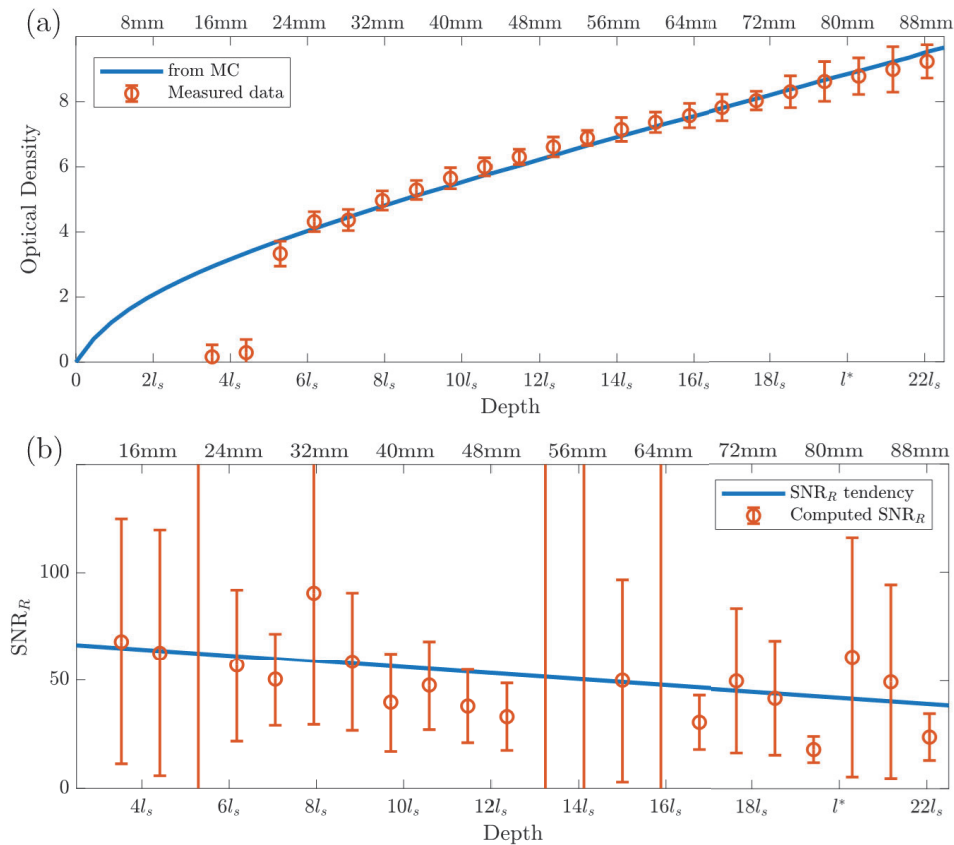


Fig. 16. Practical results related to measurement of the intensity propagation in the milk solution. The MC simulation that was used for comparison is based on the optical parameters $\mu_a = 0.035$ [mm^{-1}], $\mu_s = 0.25$ [mm^{-1}] and $g = 0.95$. The data points (orange) display the mean and standard deviation of the measurements ($\mu \pm \sigma$). (a) Optical density $OD = I/I_0$ as a function of the depth. Comparison of the measured data with the MC results. (b) Signal-to-noise ratio of the intensity ratio measurements ($R = I_1/I_2 \Rightarrow SNR_R = SNR_I/\sqrt{2}$) fitted by linear function (blue).

FADE capabilities

Based on the equations (16 and 17) presented in the Spatial interpolation section, we then looked at how efficiently the FADE method could determine the optical property (μ_a DPF) of the solution (Fig. 17.a). Based on the theoretical curve generated from the MC solver, it appears that the computed values manage to match the expected ones for depths greater than $9l_s$ (i.e. 36mm in the solution). Note that the noise (i.e. standard deviation) are strongly related to the way this parameter is expressed. For instance if we looked at $l_{eq} = 1/(\mu_a \text{DPF})$, the noise would have been small for shallow measurements and would have increased with the depth, which can be a more intuitive behaviour.

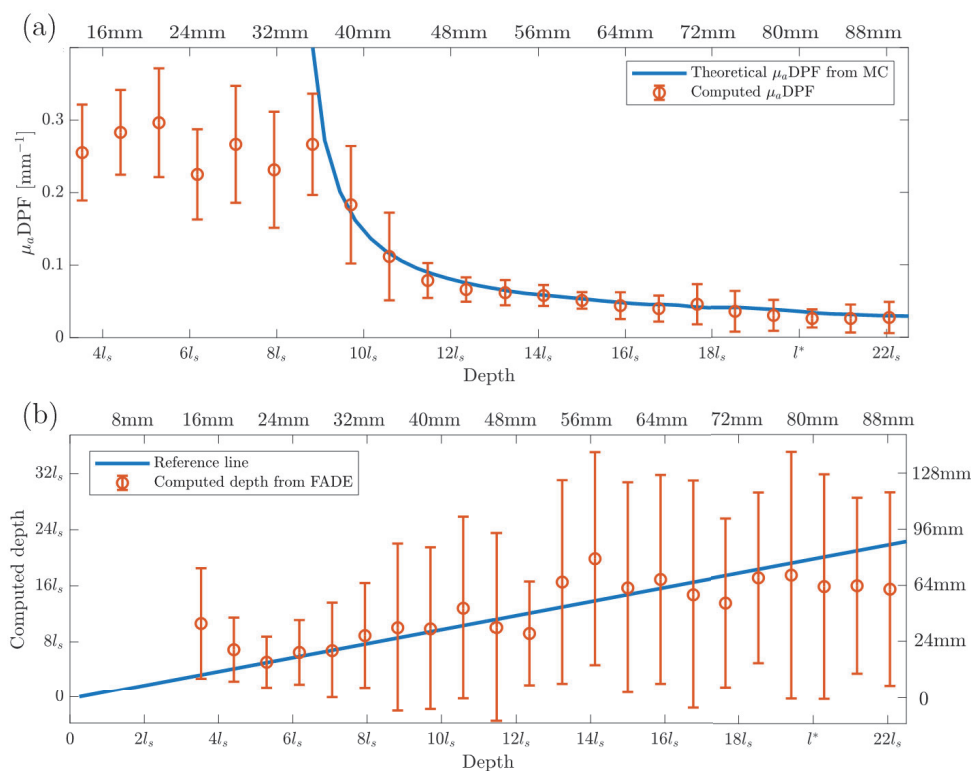


Fig. 17. Practical results related the outputs generated by the FADE method. The MC simulation that was used for comparison is based on the optical parameters $\mu_a = 0.035$ [mm^{-1}], $\mu_s = 0.25$ [mm^{-1}] and $g = 0.95$. The data points (orange) display the mean and standard deviation of the measurements ($\mu \pm \sigma$). (a) Measurement of the μ_a DPF value using Eq. (16) and compared with the theoretical value obtained from the MC simulation. (b) Depth measurements computed from Eq. (17) and compared with the expected value.

We also investigated if the FADE method was actually able to return the absolute depth position of the probe (Fig. 17.b) without any a priori on the medium properties by using only Eq. (17) and the 3D-FADE procedure (c.f. Fig. 5). The related figure shows very noisy measurements whose means seem to match the expected value.

3D tracking

Finally, we decided to investigate what was the best way to accurately and rapidly localize the probe. Since the depth measurements using FADE are too noisy to generate a stable value without a lot of averaging, we chose not to use it for that last part. Instead, to achieve a fast tracking, we use the measured intensity as an input to inverse the DE (Eq. (2)) function (r as a function of I). This might seem a simpler solution than FADE but it actually requires to perfectly know the medium's optical properties beforehand (not needed with FADE) and the Lambert-W function [35] has to be used to inverse the DE.

More than 1'300 measurements were manually done to characterise the capabilities of the device for each possible x,y,z locations. With that, we could determine the accuracy and related noise of the x_f, y_f and z_f (i.e. probe's depth) computed values as a function of the x, y or z (i.e. depth) position. This results in 9 plots for the accuracy and 9 plots for the noise. Here we will only present the ones that depicts an interesting behaviour of the system. All the original plots are available in the [Supplementary Section 1](#). Note that in most cases, the respective measurements of x_f and y_f were very similar due the system's symmetries. We remind that these are found by spatially interpolating the single-pixel image (see [Spatial interpolation](#)).

Absolute error

Many different things are worth mentioning when looking at the absolute error results (Fig. 28). First, we notice that the error on y_f is strongly dependent on the y -position of the probe (Fig. 28.a). It appears that the error is minimum when the probe is aligned with one of the sources (red squares) and can go as high as $p/2$ (where p is the spacing of the sources) when the probe is exactly in between two sources. Some more measurements to find the effect of p on

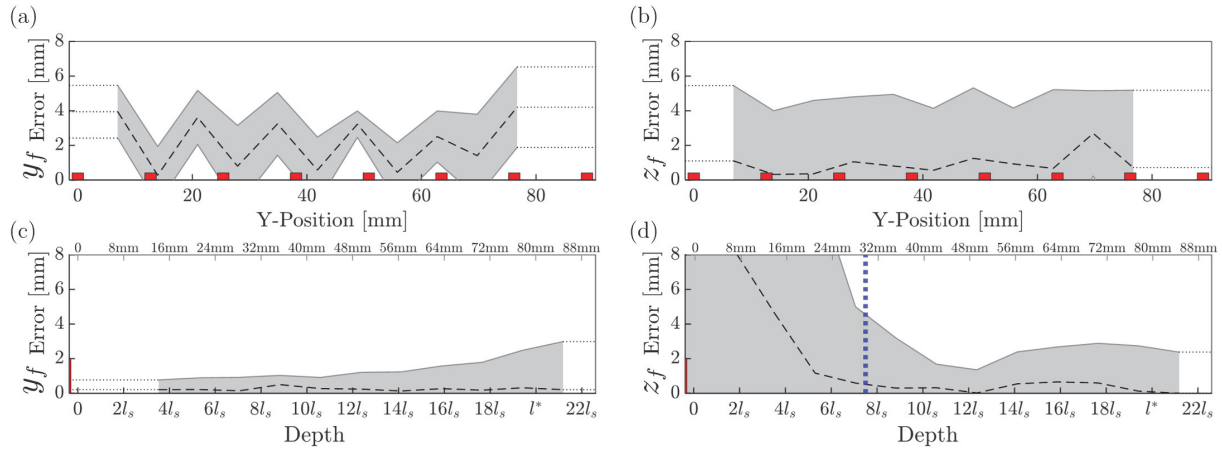


Fig. 18. Localization absolute error based on $11 \times 11 \times 11$ measurements (equally spaced on each axis, 40 data points for each) done in the 5‰ milk solution. The dashed line corresponds to the mean error (when the data points are average over the two axis other than the abscissa), equivalent to the **inaccuracy** of the measurements. Similarly, the shaded area corresponds to the standard deviation and is equivalent to the **imprecision** of the measurements. The measurements on the depth are shown in units of l_s as well as [mm]. (a) y_f error vs y position. (b) z_f error vs y position. (c) y_f error vs depth. (d) z_f error vs depth, where the blue line show the threshold value.

the maximum error could be interesting to do. We will simply assume that the maximum error is equal to $p/2$, but much more parameters are probably involved. When compared to the depth, the computed y_f remains accurate even for greater depth, but its precision seems to worsen quadratically (Fig. 28.c). Looking at the z_f error vs depth (Fig. 28.d), we find very inaccurate and imprecise results for shallow position of the probe. It is only after a depth threshold of around $8l_s$ (i.e. 32mm) that we start to obtain decent results, which is very similar (and most likely linked) to the threshold observed for the intensity propagation measurement (Fig. 16.a).

Noise

A few interesting observations can also be made from the measure of the noise (Fig. 19). First, thanks to a prefiltering at the microcontroller level, the noise is rather low in comparison to the measurement's imprecision. The noise also seems to be stable regardless of the y (or x) position of the probe. The only noticeable variation is on the y_f (thus also x_f) noise which appears to also quadratically increase with the depth (Fig. 19.c).

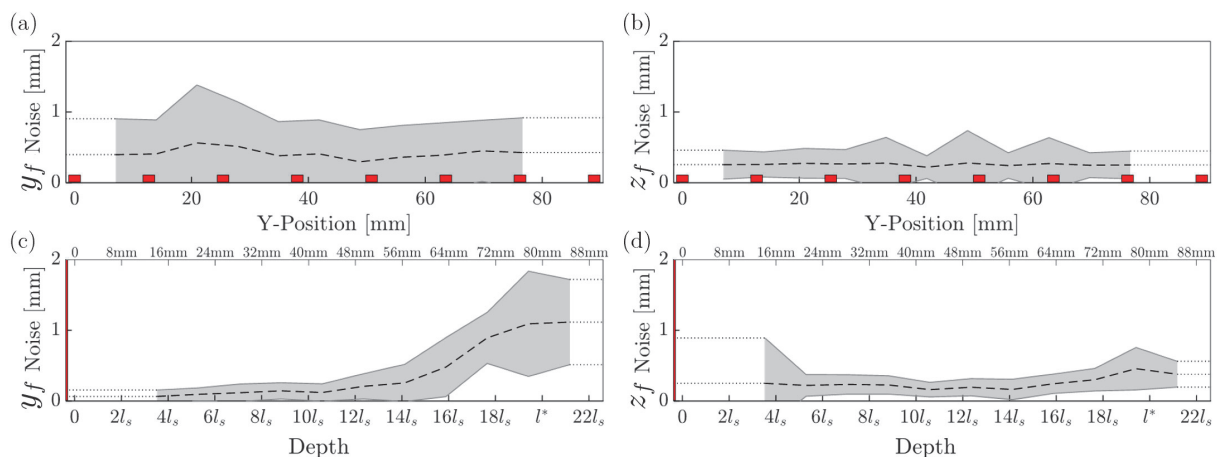


Fig. 19. Noise of the measurements, based on the same data as Fig. 28 except that in this case the standard deviation (instead of mean) has been computed from the raw 40 data points of each measurements. Note that measured data were already preprocessed (trust factor based filtering) by the microcontroller, leading to a first noise reduction. The dashed lines represent then the mean amplitude of the noise and the shaded area its deviation. (a) y_f noise vs y. (b) z_f noise vs y. (c) y_f noise vs depth. (d) z_f noise vs depth.

Discussion

Our goal was to find if it was possible to localize a fluorophore accurately and without any knowledge on the complex medium surrounding the particle. The FADE's set of equations as well as other approaches have been practically tested on a proof of concept device and their results will now be discussed.

The results indicate that we might be on the right track. When looking at the computed depth using FADE (Fig. 17.b), it appears that the mean value of the measurements matches with the expected output, but remains very noisy. The usual deviation is around $\pm 15 \cdot l_s$ (i.e. $\pm 60\text{mm}$), meaning that a strong averaging is required to obtain usable information. This issue was to be expected. In fact, using the simulations we showed that a minimum SNR_R of 100 was needed to obtain an accurate output, and this was even without considering the error on the xy position. Looking at the SNR we obtained in our measurements (Fig. 16), it clearly appears that we are not able to meet that requirement.

The obtained SNR_R is nevertheless high enough to accurately measure the intensity attenuation in the medium (Fig. 16.a) and to obtain a very low response time of its variation when the probe is moved. We then showed that by using the DE inverse function it was possible to efficiently determine the depth of the probe (Fig. 28.d) but this requires to know the medium's optical properties.

One recurrent behaviour is the inaccuracy observed on shallow measurements, for both FADE and the direct intensity measurements. The error on the intensity for short source-detector distance is probably related to the saturation of the photodiode, which could probably be avoided by using another sensor. Also, since the sources we use are not perfectly isotropic, only the light emitted by one source will be sensed if the probe location is too shallow ($R \rightarrow \infty$). This means that the FADE procedure is useless in that case as the results of the FADE's equations (Eq. 16 and 17) are undetermined (i.e. $0/0$). This effect is also visible in the noise formulae (Eq. 18 and 19), where a high R leads to high noises. Having $R = 1$ would theoretically minimize the noise but it would once more lead to undetermined results (cf. Eq. 16 and 17). In practice it appeared that the best results were obtained for $2 < R < 100$.

To determine the xy position of the probe, we showed that the spatial interpolation solution was giving very good results (Fig. 28.a,c) that could further be improved if a smaller source spacing p was used. The main limitation arises when the probe is located deep in the medium. Since the probe-sources distances tend to equalize for great depth, the intensity contrast is reduced ($R \rightarrow 1$) making the fitting of a two-dimensional Gaussian difficult and strongly influenced by the noise.

By using the blinking fluorophore method developed for PALM [3], the 3D localization of a single particle can lead to a full 3D image obtained by successively localizing each of the fluorophores. Even though many limitations have to be considered, our experiments demonstrate new insights for 3D imaging in complex media. In comparison to 3D-STORM, where a cylindrical lens can be used to determine the (shallow) depth information [36], our method removes the need of complicated optical elements and allows to determine the position of particles at much greater depth using only three intensity measurements. The single-pixel imaging approach also has the potential to obtain much faster results since only one sensor has to be measured (analog-to-digital conversion), the sources can be rapidly actuated and they can easily be reduced to the minimum amount required for detection. Thanks to the method developed in PALM, this single fluorophore localization can then be extended to full 3D imaging with the use of blinking fluorophores.

Achieving a high detection frame rate (i.e. $> 10\text{fps}$) was one of the main goals of this work and could find applications where a real-time feedback is required. For instance, in the case of (fluorescent) microrobot that travels inside a human body [37], it could be used to provide a passive live 3D tracking of its position by simply laying an array of sources (non invasive) on the person's skin.

Further research is required to establish whether FADE quality could be substantially improved by using better equipment and if it could perform well on biological tissues. In regard to the obtained results, our recommendations would be to find a trade-off between FADE and the inverse DE methods. In fact, by sufficiently averaging the FADE results for the depth, one could obtain an absolute reference value. Then, by utilizing the more dynamic values obtained by direct measurement of the intensity along with the (less noisy) FADE computed $\mu_a\text{DPF}$ value (i.e. the local slope of the intensity extinction curve), it would be possible to determine the relative displacement of the particle.

Conclusion

We proposed different approaches for three-dimensional localization of fluorophores in complex media. We introduced FADE (a set of equations derived from the MBLL) that can, based on only three single-pixel measurements, determine the absolute depth of a probe (or equivalently a fluorescent particle) without any a priori on the media's optical properties. Using a proof of concept setup, we tested our theory and simulations on a milk solution with optical properties comparable to the ones of biological tissues/fluids. Due to our limited equipment, the obtained results were pretty noisy and not usable yet. They nonetheless showed the expected tendencies and gave us confidence that this method could one day lead to real applications.

Contributions

FdG is the main author of this work, built the setup and did the measurements. BB gave the initial idea and closely supervised the work all along. CY provided fortnightly feedback, gave very useful advice and supervised the work. CM verified the overall smooth running of the project.



Code availability

The codes used in this work are available from the main author upon request.

Supplementary information

Supplementary information is available for this work at the end of the journal, starting page 29.

References

1. S. Yoon, M. Kim, M. Jang, Y. Choi, W. Choi, S. Kang, and W. Choi, "Deep optical imaging within complex scattering media," *Nat. Rev. Phys.* **2**, 141–158 (2020).
2. M. G. Giacomelli and A. Wax, "Imaging beyond the ballistic limit in coherence imaging using multiply scattered light," *Opt. express* **19**, 4268–4279 (2011). Publisher: Optical Society of America.
3. E. Betzig, G. H. Patterson, R. Sougrat, O. W. Lindwasser, S. Olenych, J. S. Bonifacino, M. W. Davidson, J. Lippincott-Schwartz, and H. F. Hess, "Imaging Intracellular Fluorescent Proteins at Nanometer Resolution," *Science* **313**, 1642–1645 (2006). Publisher: American Association for the Advancement of Science _eprint: <https://science.sciencemag.org/content/313/5793/1642.full.pdf>.
4. J. Xia, J. Yao, and L. V. Wang, "Photoacoustic tomography: principles and advances," *Electromagn. waves (Cambridge, Mass.)* **147**, 1–22 (2014).
5. Y. H. M.D. and Y. Yamada, "Overview of diffuse optical tomography and its clinical applications," *J. Biomed. Opt.* **21**, 1 – 11 (2016).
6. A. Turpin, G. Musarra, V. Kapitany, F. Tonolini, A. Lyons, I. Starshynov, F. Villa, E. Conca, F. Fioranelli, R. Murray-Smith, and D. Faccio, "Spatial images from temporal data," *Optica* **7**, 900–905 (2020).
7. M. P. Edgar, G. M. Gibson, and M. J. Padgett, "Principles and prospects for single-pixel imaging," *Nat. Photonics* **13**, 13–20 (2019).
8. P. Wang, S. R. Arridge, and M. Jiang, "Radiative transfer equation for media with spatially varying refractive index," *Phys. Rev. A* **90**, 023803 (2014).
9. C. Dogbe, "The radiative transfer equations: diffusion approximation under accretiveness and compactness assumptions," *Comput. & Math. with Appl.* **42**, 783 – 791 (2001).
10. S. Fantini, M. A. Franceschini, and E. Gratton, "Semi-infinite-geometry boundary problem for light migration in highly scattering media: a frequency-domain study in the diffusion approximation," *J. Opt. Soc. Am. B* **11**, 2128–2138 (1994).
11. R. C. Haskell, L. O. Svaasand, T.-T. Tsay, T.-C. Feng, M. S. McAdams, and B. J. Tromberg, "Boundary conditions for the diffusion equation in radiative transfer," *J. Opt. Soc. Am. A* **11**, 2727–2741 (1994).
12. D. Contini, F. Martelli, and G. Zaccanti, "Photon migration through a turbid slab described by a model based on diffusion approximation. i. theory," *Appl. Opt.* **36**, 4587–4599 (1997).
13. A. Zhang, D. Piao, C. F. Bunting, and B. W. Pogue, "Photon diffusion in a homogeneous medium bounded externally or internally by an infinitely long circular cylindrical applicator. i. steady-state theory," *J. Opt. Soc. Am. A* **27**, 648–662 (2010).
14. T. Y. Chow, "What is a closed-form number?" *The Am. Math. Mon.* **106**, 440–448 (1999).
15. D. T. Delpy, M. Cope, P. van der Zee, S. Arridge, S. Wray, and J. Wyatt, "Estimation of optical pathlength through tissue from direct time of flight measurement," *Phys. Medicine Biol.* **33**, 1433–1442 (1988).
16. L. Kocsis, P. Herman, and A. Eke, "The modified beer–lambert law revisited," *Phys. Medicine Biol.* **51**, N91–N98 (2006).
17. M. Bhatt, K. R. Ayyalasamayajula, and P. K. Yalavarthy, "Generalized Beer–Lambert model for near-infrared light propagation in thick biological tissues," *J. Biomed. Opt.* **21**, 1 – 11 (2016).
18. M. A. Kamran, M. M. N. Mannann, and M. Y. Jeong, "Differential path-length factor's effect on the characterization of brain's hemodynamic response function: A functional near-infrared study," *Front. Neuroinformatics* **12**, 37 (2018).
19. D. Piao, R. L. Barbour, H. L. Graber, and D. C. L. M.D., "On the geometry dependence of differential pathlength factor for near-infrared spectroscopy. I. Steady-state with homogeneous medium," *J. Biomed. Opt.* **20**, 1 – 14 (2015).
20. L. Kocsis, P. Herman, and A. Eke, "The modified beer–lambert law revisited," *Phys. Medicine Biol.* **51**, N91–N98 (2006).
21. M. J. Rust, M. Bates, and X. Zhuang, "Sub-diffraction-limit imaging by stochastic optical reconstruction microscopy (STORM)," *Nat. Methods* **3**, 793–796 (2006).

22. A. Boniface, B. Blochet, J. Dong, and S. Gigan, "Noninvasive light focusing in scattering media using speckle variance optimization," *Optica* **6**, 1381 (2019).
23. R. S. Tucker, G. Eisenstein, and S. K. Korotky, "Optical time-division multiplexing for very high bit-rate transmission," *J. Light. Technol.* **6**, 1737–1749 (1988).
24. K. Nosu, H. Toba, and K. Iwashita, "Optical fdm transmission technique," *J. Light. Technol.* **5**, 1301–1308 (1987).
25. G. Kloos, *Applications of Lock-in Amplifiers in Optics* (SPIE, 2018).
26. J. W. Goodman, "Some fundamental properties of speckle*," *J. Opt. Soc. Am.* **66**, 1145–1150 (1976).
27. L. I. Goldfischer, "Autocorrelation function and power spectral density of laser-produced speckle patterns," *J. Opt. Soc. Am.* **55**, 247 (1965).
28. M. M. Qureshi, J. Brake, H.-J. Jeon, H. Ruan, Y. Liu, A. M. Safi, T. J. Eom, C. Yang, and E. Chung, "In vivo study of optical speckle decorrelation time across depths in the mouse brain," *Biomed. Opt. Express* **8**, 4855 (2017).
29. H. Ruan, Y. Liu, J. Xu, Y. Huang, and C. Yang, "Fluorescence imaging through dynamic scattering media with speckle-encoded ultrasound-modulated light correlation," *Nat. Photonics* **14**, 511–516 (2020).
30. L. Shi, L. A. Sordillo, A. Rodríguez-Contreras, and R. Alfano, "Transmission in near-infrared optical windows for deep brain imaging," *J. Biophotonics* **9**, 38–43 (2015).
31. B. Aernouts, R. V. Beers, R. Watté, T. Huybrechts, J. Lammertyn, and W. Saeys, "Visible and near-infrared bulk optical properties of raw milk," *J. Dairy Sci.* **98**, 6727–6738 (2015).
32. C. Veenstra, D. E. Every, W. Petersen, J. B. van Goudoever, W. Steenbergen, and N. Bosschaart, "Dependency of the optical scattering properties of human milk on casein content and common sample preparation methods," *J. Biomed. Opt.* **25**, 1 (2020).
33. H. D. Downing and D. Williams, "Optical constants of water in the infrared," *J. Geophys. Res.* **80**, 1656–1661 (1975).
34. R. Röttgers, R. Doerffer, D. McKee, and W. Schönfeld, "Pure water spectral absorption, scattering, and real part of refractive index model algorithm technical basis document," (2010).
35. E. W. Weisstein, "Lambert w-function," <https://mathworld.wolfram.com/> (2002).
36. B. Huang, W. Wang, M. Bates, and X. Zhuang, "Three-dimensional super-resolution imaging by stochastic optical reconstruction microscopy," *Science* **319**, 810–813 (2008).
37. D. Jang, J. Jeong, H. Song, and S. K. Chung, "Targeted drug delivery technology using untethered microrobots: a review," *J. Micromechanics Microengineering* **29**, 053002 (2019).

Build your own experiments

EE005 - Introduction to waves

In the context of setting up a new course for the California Institute of Technology (Caltech), I was asked to design several practical experiments that each student could work on. The goal was, for most of the experiments, to mail them a kit containing everything they would need to build it on their own and investigate all the different concepts introduced during the class. This course is about waves in all their forms, such as mechanical (pendulums, oscillators, etc.), acoustical or electromagnetic. The related experiment had to be easy to assemble, cost-effective and using only standard components. To meet these requirements, I decided to get myself a laser cutter that was used to create most of the custom parts. That way all the design files could easily be sent to Caltech and manufactured at their own facilities. Here we will briefly present the work of many months of design and experimentation to finally come up with 5 experiments the Caltech's freshman students will be working on. I have also helped Prof. Yang writing the lecture notes associated with these experiments and designing the questions/answers.

Mass-spring experiment

The first experiment the students will receive consists of two simple harmonic oscillators (SHO) that can be coupled together. This allow the students to study the concepts of oscillation, damping, resonance and mode coupling.

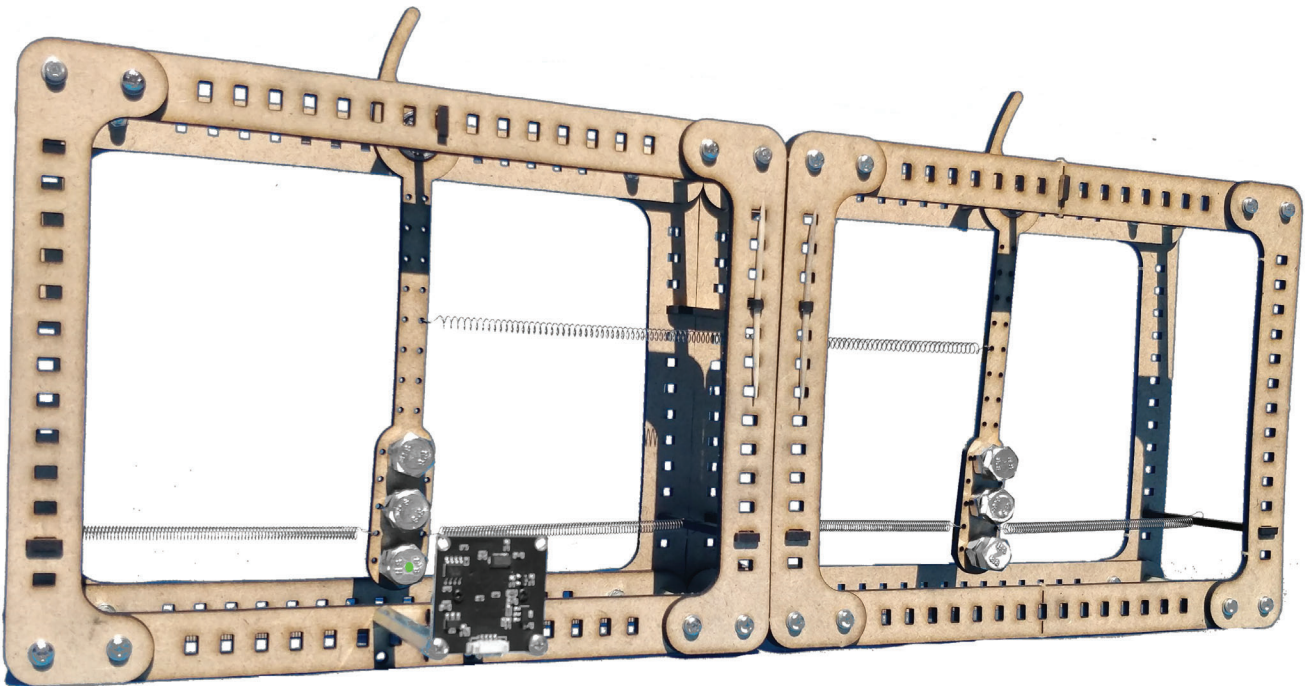


Fig. 20. Mass-spring experiment for the EE005 seminar. It comprises two simple harmonic oscillators that can be coupled by the middle spring. Each pendulum is linked to the frame with grooved ball bearings. The masses are made out of M8 screws and nuts and weight around 100 grams per pendulum. The main springs have a constant of 20N/m. All the frame is made out of laser cut 3mm MDF and is assembled using simple M3 screws and nuts.

In order for the students to visualize sinusoidal oscillations, determine the frequency and observe the damping, a provided 120fps camera (*OV2710*, \$17) can be attached on the SHO frame. By taping a little green dot on the oscillator, a custom Matlab graphical user interface (GUI) can track the motion and display the desired parameters. Since the pendulum oscillates at around 3Hz, a minimum of around 60Hz is required to properly record the motion. This rate can be modified in the GUI.

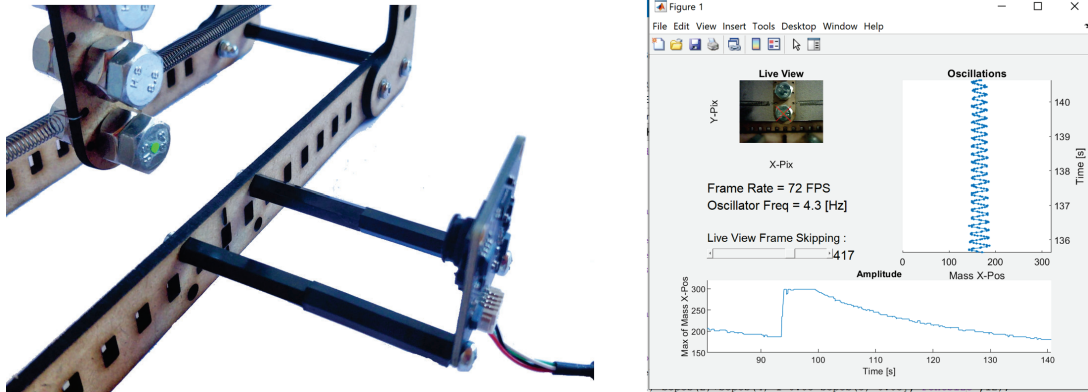


Fig. 21. Camera mounting on the frame and screenshot of the Matlab's GUI execution.

To make the most compact package that could be sent to the students, the laser cut part were assembled together in an A4 format and all the components stored in between.

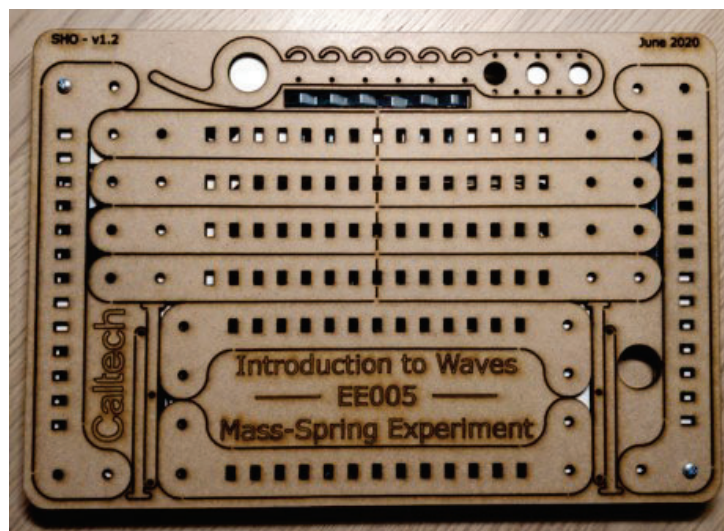


Fig. 22. Mass-spring experiment kit containing all the components to build the experiment and ready to be sent.

Twenty SHO chain

An other SHO related experiment has also been developed, but this time with 20 coupled SHO. This will serve as a demonstration for the class and the students can ask the TAs to try different things on this setup. The main goal is for them to see the propagation of a wave through all the pendulums and to verify if its velocity matches with the theory.

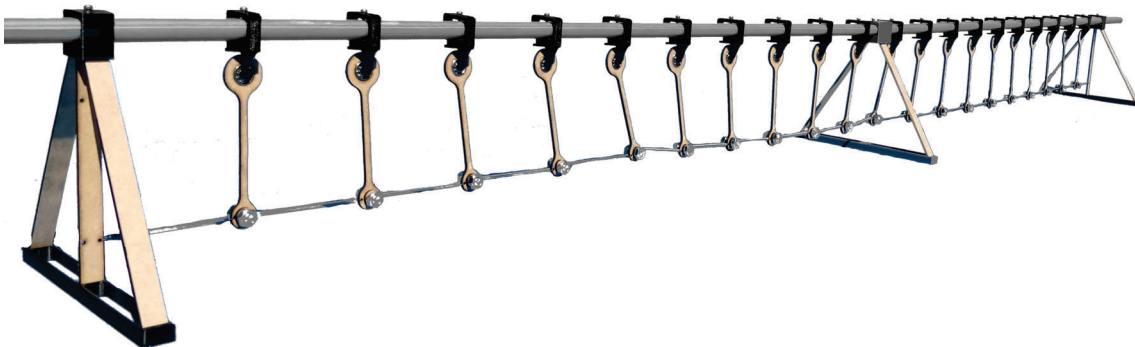


Fig. 23. Setup for the 20 coupled SHO demonstration (2.2m long)

Sound waves and arduino

In this second experiment, the students will be asked to build an electrical circuit to record and filter the incoming sound waves. The goal of this lesson is to show them the relation between the time content and the frequency content. The Fourier transformation is also introduced. To build this experiment, they are provided with an Arduino Uno, a breadboard, a microphone and various electronic components.

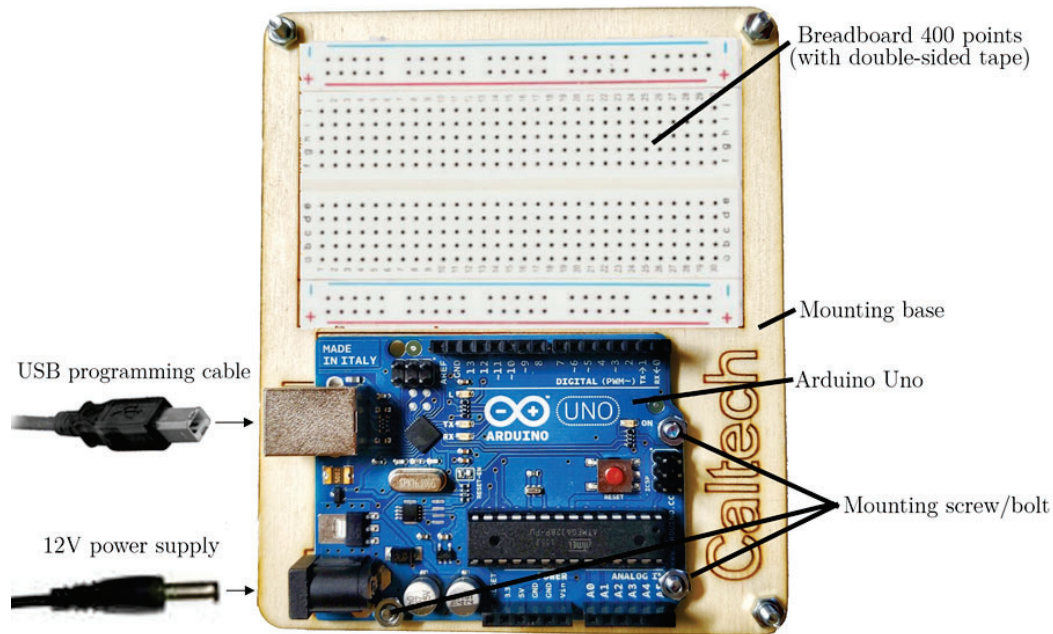


Fig. 24. Setup for the Arduino sound wave experiment with the custom laser cut mounting base

The microphone data are then transmitted to Matlab (via UART) for processing. Another custom GUI has been developed for this experiment, this time to display the time and frequency domain amplitudes of the sound waves the microphone is sensing in real time. They can also start to record sound and the recordings will be displayed in the same way. Since the GUI will be running on their computer, they will be able to use their PC's speakers to listen to these recordings with and without filtering.

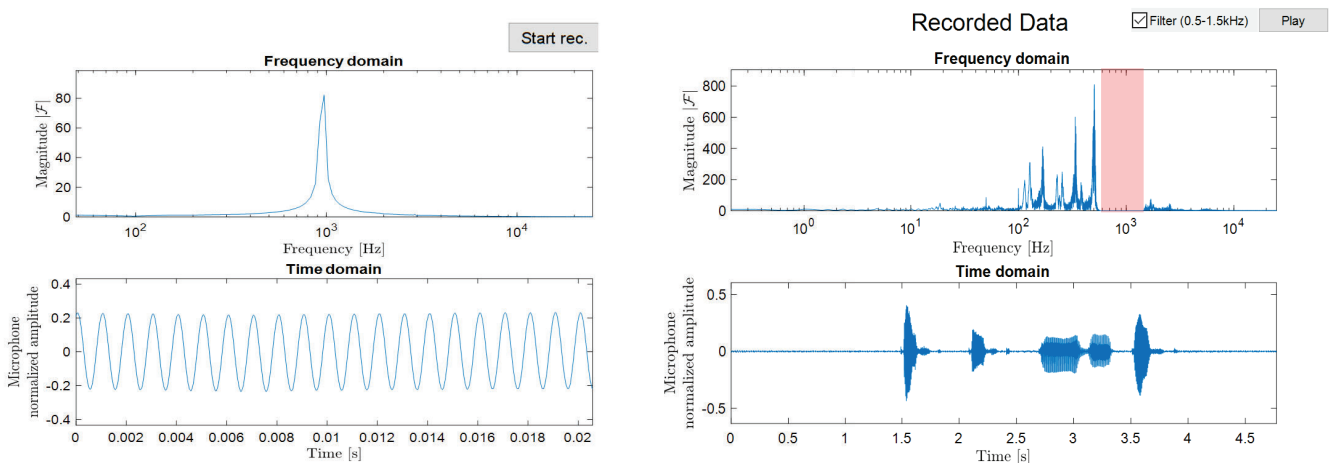


Fig. 25. Live and recorded sound wave data visualized in the custom Matlab GUI.

Instead of numerical filtering, they are then asked to make a simple RC low pass filter on their breadboard and to look at its effect on the GUI.

Forced oscillators and wine glass breaking

For this third experiment, the students are asked to study the effect of a forced oscillator and resonant frequency on a wine glass. The resonant frequency of the glass is determined using the setup of the previous experiment. Two compression speaker will be used to generate the frequencies that will drive the motion of the wine glass. If everything is done right, they should be able to break it. Since two speakers are used, they will also study the concept of interference and observe what happens when the speakers' frequencies are in phase and out of phase.

A Basler 750fps camera (*acA640-750um*) is used to visualize the glass motion. By setting the frame rate of the camera close to the resonant frequency of the glass, the glass deformation can be seen in real time thanks to the stroboscopic effect.



Fig. 26. Setup for the glass breaking experiment, comprising a laser cut sound-proof box, two compression speakers and a 750fps camera.

Smoke vortex cannon

The last experiment is about a wave that is not really a wave. It is about the torus-shaped vortices that spin around themselves and that could theoretically maintain their shape and propagate to infinity in the absence of friction and turbulence. The students will be asked to design such a vortex generator and to compete with their other classmates to see which design can knock down plastic cups the furthest. We also tried to find the best parameters to build such a cannon and came up with a 3D printed design that the students can take as reference. This simple design was able to move objects more than 10m away.



Fig. 27. Design of a simple DIY smoke vortex cannon. The barrel is 3D printed and a cut balloon is used as membrane.

Supplementary Information

1. System characterisation (full results)

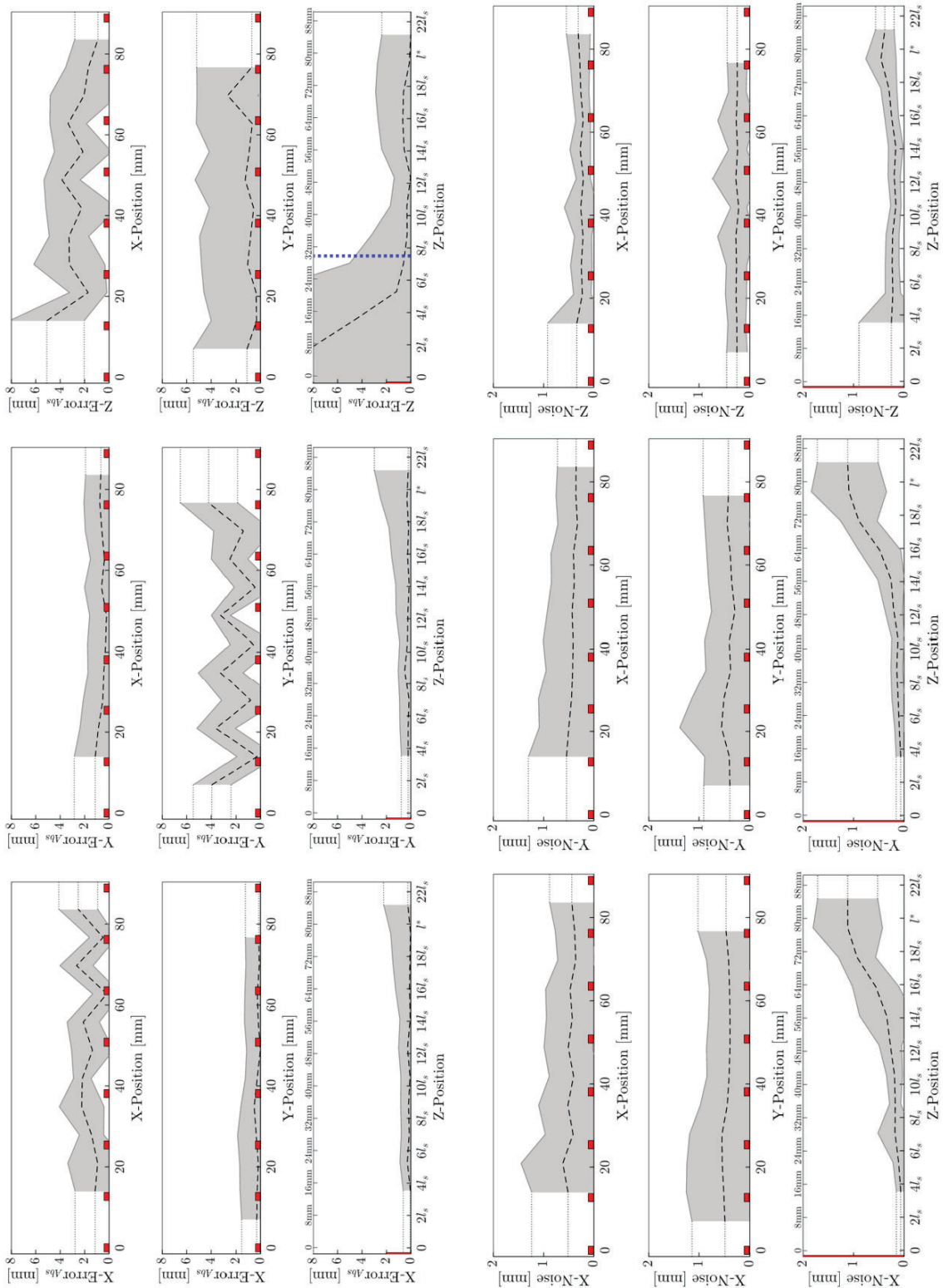


Fig. 28. Full localization results, based on the 11x11x11 measurements done in the 5%_{cc} milk solution. The dashed line corresponds to the mean error or mean noise (when the data points are average over the two axis other than the abscissa) and the shaded area corresponds to the standard deviation.

2. Derivation of the temporal speckles superposition formula

In the following, we will compute the resulting decorrelation function $g_{2,tot}(t)$ coming from the superposition of the two temporal speckles.

We send two incident dynamic speckle fields E_i , $i \in [1, 2]$ with known intensity decorrelation function $g_{2,i}(t)$.

From Siegert relationship

$$g_{2,i}(t) = 1 + |g_{1,i}(t)|^2 \quad \Rightarrow \quad |g_{1,i}(t)| = \sqrt{g_{2,i}(t) - 1} = \sqrt{g'_{2,i}(t)} \quad (32)$$

where $g_{2,i}(t)$ by convention varies between 1 and 2. We find it more convenient to work with $g'_{2,i}(t) = g_{2,i}(t) - 1$ which varies between 0 and 1. $g_{1,i}$ is the field decorrelation function and is a complex function. By definition

$$g_{1,i}(t_0) \equiv \frac{\langle E(t) \cdot E^*(t - t_0) \rangle}{\langle |E(t)|^2 \rangle} \quad (33)$$

Based on the previous equation and defining $E(t) = E_{tot}(t) = E_1(t) + E_2(t)$ and $\langle |E_i|^2 \rangle = I_i$, we get

$$g_{1,tot}(t) = \frac{\langle (E_1 + E_2)(t) \cdot (E_1 + E_2)^*(t - t_0) \rangle}{\langle |(E_1 + E_2)|^2 \rangle} \quad (34)$$

If we assume E_1 and E_2 to be uncorrelated, meaning $\langle E_i(t) \cdot E_j^*(t - t_0) \rangle = 0$ for $i \neq j$, we obtain

$$g_{1,tot}(t) = \frac{\langle E_1(t) \cdot E_1^*(t - t_0) \rangle}{I_1 + I_2} + \frac{\langle E_2(t) \cdot E_2^*(t - t_0) \rangle}{I_1 + I_2} = \frac{I_1 \cdot g_{1,1}(t) + I_2 \cdot g_{1,2}(t)}{I_1 + I_2} \quad (35)$$

where $g_{1,tot}(t)$ is the field decorrelation function for the superposition of two dynamic speckles. Using the Siegert relationship from Eq. (32) we then obtain the decorrelation function for the two superposed speckles as

$$g'_{2,tot}(t) = \left| \frac{I_1 \cdot g_{1,1}(t) + I_2 \cdot g_{1,2}(t)}{I_1 + I_2} \right|^2 = \frac{\left| I_1 \cdot \sqrt{g'_{2,1}(t)} \cdot e^{i\phi_1 t} + I_2 \cdot \sqrt{g'_{2,2}(t)} \cdot e^{i\phi_2 t} \right|^2}{(I_1 + I_2)^2} \quad (36)$$

And finally by assuming that $g_{1,i}(t)$ is real

$$g'_{2,tot}(t) = \left(\frac{I_1 \cdot \sqrt{g'_{2,1}(t)} + I_2 \cdot \sqrt{g'_{2,2}(t)}}{I_1 + I_2} \right)^2 \quad (37)$$

where $g'_{2,i}(t)$ can have various shapes depending on what generated the medium's motion. For instance, if the variations are due to Brownian motion

$$g'_{2,i}(t) = e^{-t/\tau_i} \quad \text{for } t > 0 \quad (38)$$

where τ_i is the decorrelation time.

3. Algorithms for generation of temporal speckles and computation of R

Example of main code:

```

1 % Exemple code for speckle generation and intensity riation computation
2 duration = 1;% [s]
3 fps = 200;
4 pixels = 64;
5 speckle_size = 1;
6 g2_model = @(tau, x) exp(-x./tau); % Brownian motion
7 needed_tau1 = 50e-3;% [s]
8 needed_tau2 = 500e-3;% [s]
9 I1 = 1; I2 = 2;
10
11 % Generate first temporal speckle
12 E1 = genTempSpeck(needed_tau1,duration,fps,pixels,speckle_size,g2_model);
13 % Generate second temporal speckle
14 E2 = genTempSpeck(needed_tau2,duration,fps,pixels,speckle_size,g2_model);
15 % Compute the total speckle electric field
16 Etot = sqrt(I1)*E1 + sqrt(I2)*E2;
17 % Compute R
18 [tau,R] = findR(Etot,fps,tau1,tau2,g2_model);

```

Temporal speckle electric field generation function:

```

1 % Function to generate the temporal speckle electric field
2 % g2 is the autocorrelation function related to one temporal speckle
3 % For Brownian motion, g2 = @(t) exp(-t./tau);
4 function Efield = genTempSpeck(tau,duration,fps,pixels,speckle_size,g2)
5 % 2D low pass to generate speckle with grains equal to speckle_size
6 [X,Y] = meshgrid(1:pixels,1:pixels); % image vectors
7 C = floor(pixels/2+1); % image center
8 r = abs(X-C + 1i*(Y-C)); % distance of every pixels from the center
9 CTF = r<pixels/(2*speckle_size); % circle around center of image
10
11 % initial random phase of the speckles
12 phase = 2*pi*randn(pixels,pixels);
13 Efield = zeros(pixels,pixels,fps*duration);
14 for frame=1:fps*duration
15 % update the standard deviation of the random phase for each frame
16 std = sqrt(log(g2(tau,(frame-1)/fps)) - log(g2(tau,frame/fps)));
17 phase = phase + std*randn(pixels,pixels);
18 Efield(:,:,frame) = fft2(exp(1i*phase).*CTF);%
19 end
20 end

```

Function to compute R:

```

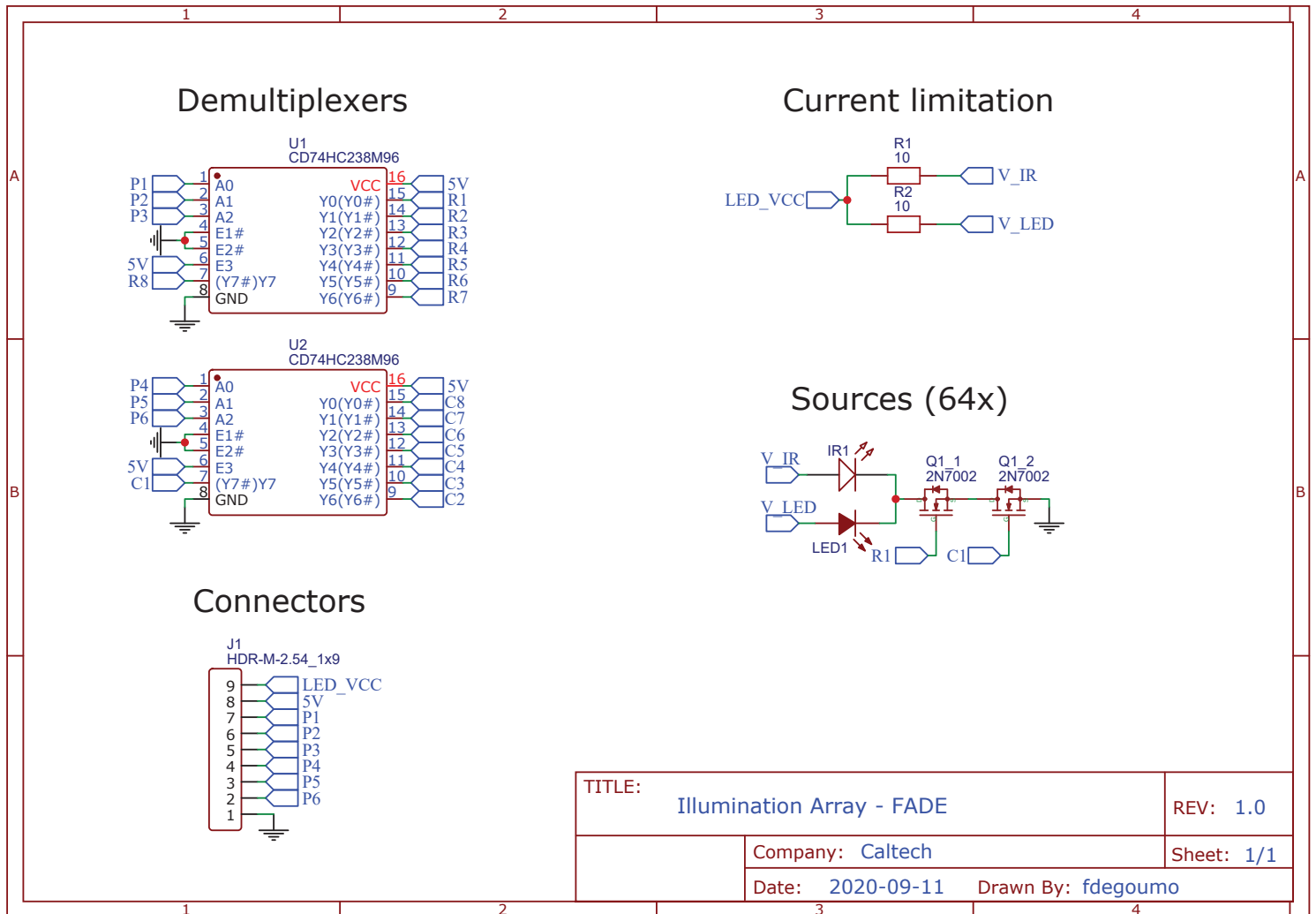
1 % Computes the intensity ratio and the total decorrelation time of
2 % of two superposed temporal speckles
3 function [tau, R] = findR(Efield, fps, tau1, tau2, g2_model)
4 frame = size(Efield,3);
5 duration = frame/fps;
6
7 I = abs(Efield.^2);
8
9 g2 = zeros(frame,1);
10 for i=1:frame
11 g2(i) = -1 + mean2(I(:, :, i) .* I(:, :, i)) / (mean2(I(:, :, 1)) * mean2(I(:, :, i)));
12 end
13
14 % Computes R by fitting of the theoretical g2_tot curve
15 t = linspace(0,duration, frame);
16 fitfun = fittype(@(i1,i2,a,b,x) (a.*exp(-x./b))+(1/(i1 + i2)^2)...
17 *abs(i1.*sqrt(g2_model(tau1,x)) + i2.*sqrt(g2_model(tau2,x))).^2);
18 fitted = fit(t',g2,fitfun, 'StartPoint',[1 1 0 1]);
19 I_R = coeffvalues(fitted);
20 R = I_R(1)/I_R(2);
21
22 % Compute tau_tot from the initial slope
23 D = diff(g2)*fps;
24 [tau,I] = min(D);
25 M = mean(D(max(I-2,1):I+2));
26 tau = -1/M;
27 end

```

4. PCB Schematics

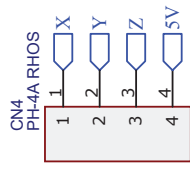
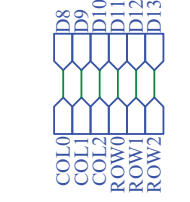
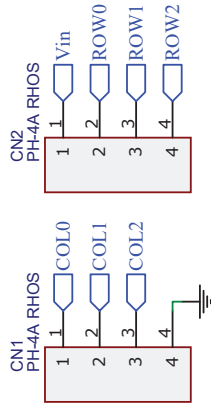
We present the most important PCB schematics that we designed for the FADE setup.

1. Illumination array schematic:

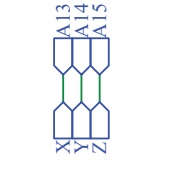


2. Control board schematic:

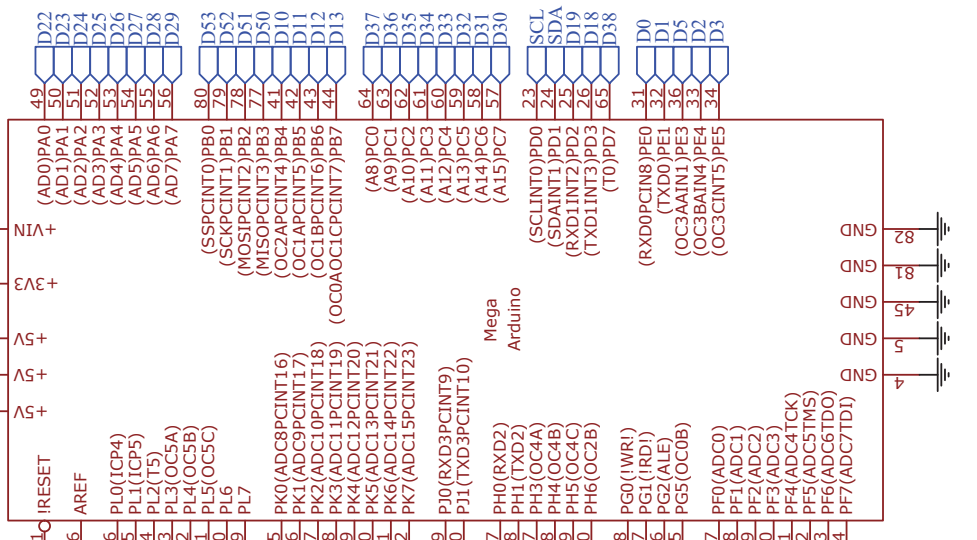
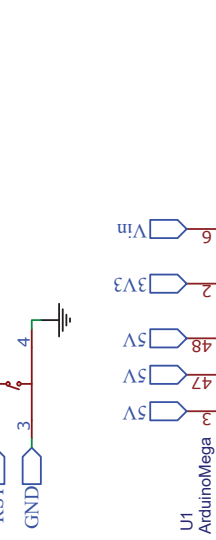
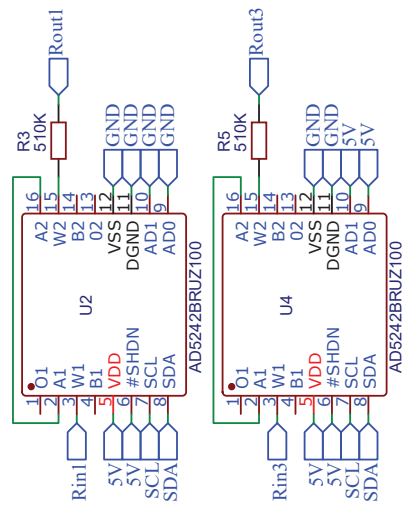
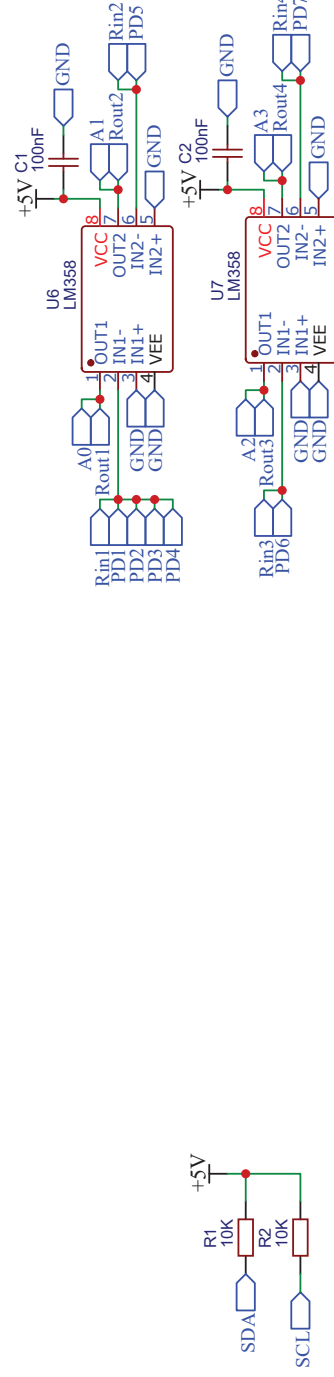
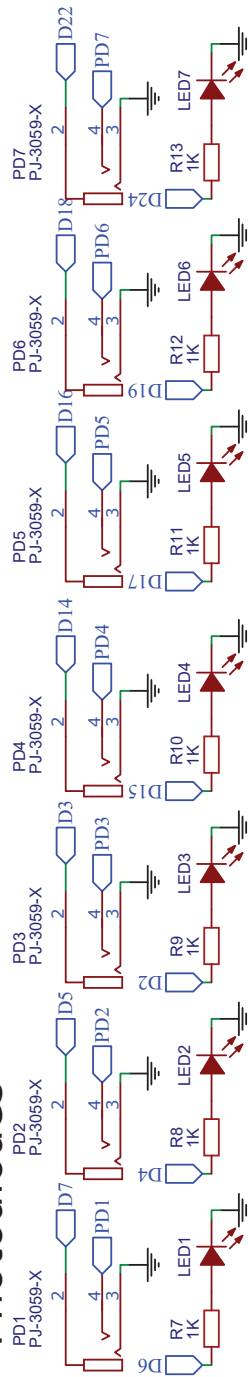
LED Array



GroundTruth



Photodiodes



TITLE: FADE control board hat		REV: 1.0
Company: Caltech		Sheet: 1/1
Date: 2020-08-21		Drawn By: fdougoumo